# High Resolution Measurements of Supersonic Mixing and Combustion in Coflowing Turbulent Jets

Werner J.A. Dahm and James F. Driscoll

**19991006 136**

**Laboratory for Turbulence and Combustion (LTC)**

www.engin.umich.edu/dept/aero/ltc

Department of Aerospace Engineering
The University of Michigan
Ann Arbor, MI 48109-2140

*August 1998*

AFRL-SR-BL-TR-99-

# REPORT DOCUMENTATION PAGE

*00 75*

| 1. AGENCY USE ONLY *(Leave blank)* | 2. REPORT DATE<br>August 28, 1998 | 3. REPORT TYPE AND DATES COVERED<br>Final Technical Report |
|---|---|---|

| 4. TITLE AND SUBTITLE<br>(U) High Resolution Measurements of Supersonic Mixing and Combustion in Coflowing Turbulent Jets | 5. FUNDING NUMBERS<br><br>PE – 61102F<br>PR – 2308<br>SA – BS<br>G – F49620-95-1-0115 |
|---|---|
| **6. AUTHOR(S)**<br><br>W.J.A. Dahm and J.F. Driscoll | |

| 7. PERFORMING ORGANIZATION(S) AND ADDRESS(ES)<br><br>Department of Aerospace Engineering<br>The University of Michigan<br>Ann Arbor, MI  48109-2140 | 8. PERFORMING ORGANIZATION<br>REPORT NUMBER |
|---|---|

| 9. SPONSORING ORGANIZATION NAME(S) AND ADDRESS(ES)<br><br>AFOSR/NA<br>801 North Randolph Street<br>Arlington, VA  22203-1977 | 10. SPONSORING ORGANIZATION<br>REPORT NUMBER |
|---|---|

11. SUPPLEMENTARY NOTES

| 12a. DISTRIBUTION / AVAILABILITY STATEMENT<br><br>Approved for public relese; distribution is unlimited | 12b. DISTRIBUTION CODE |
|---|---|

13. ABSTRACT *(Maximum: 200 words)*

An experimental study of compressibility effects on the large scale structure and outer variable scaling laws of a coflowing turbulent jet was partially completed. Results showed distinct large scale structure and classical incompressible scaling where the convective Mach number has decreased to subsonic values. At supersonic convective Mach numbers no large scale structure was seen and incompressible scalings were dramatically modified. Experiments also showed strong effects due to oblique shock wave interactions with combustion in supersonic turbulent jets. OH PLIF imaging measurements comparing subsonic and supersonic jets documented striking differences in their mixing and combustion properties. Combined OH/CH PLIF imaging measurements found large differences in the combustion properties of jet flames created by small differences in the fuel injection design. A theoretical study of density effects due to combustion heat release on the outer variable scalings of turbulent shear flows was completed. This study produced a general methodology for predicting the changes in such quantities as growth rates, velocity decay, and entrainment and mixing rates due to heat release. Comparisons with measured heat release effects in the literature, including planar and axisymmetric jet flames as well as mixing layers, showed excellent agreement with this general approach.

| 14. SUBJECT TERMS<br><br>Turbulent Combustion; Flames | | | 15. NUMBER OF PAGES<br>57 58 |
|---|---|---|---|
| | | | 16. PRICE CODE |

| 17. SECURITY CLASSIFICATION<br>OF REPORT<br>Unclassified | 18. SECURITY CLASSIFICATION<br>OF THIS PAGE<br>Unclassified | 19. SECURITY CLASSIFICATION<br>OF ABSTRACT<br>Unclassified | 20. LIMITATION OF ABSTRACT<br>UL |
|---|---|---|---|

NSN 7540-01-280-5500

Standard Form 298 (890104 Draft)
Prescribed by ANSI Std. 239-18
298-01

# 1. Introduction

This Final Report summarizes several major findings from an experimental and theoretical investigation of various aspects of supersonic turbulent combustion. The report is divided into four major sections, each of which addresses findings from one or more aspects of this subject. In addition, a number of archival publications have resulted, in part or in whole, from the work done under this AFOSR contract. These are summarized below, and should be consulted for details on any of the sections of the present report.

Buch, K.A. and Dahm, W.J.A. (1996) Fine scale structure of conserved scalar mixing in turbulent flows. Part I. Sc » 1; Journal of Fluid Mechanics, Vol. 317, 21–71.

Buch, K.A. & Dahm, W.J.A. (1998) Experimental study of the fine-scale structure of conserved scalar mixing in turbulent flows. Part II. Sc ≈ 1. *J. Fluid Mech.* 364, 1-29.

Su, L.K. & Dahm, W.J.A. (1996) Scalar imaging velocimetry measurements of the velocity gradient tensor field at the dissipative scales of turbulent flows. Part I: Validation tests; Physics of Fluids Vol. 8 (7), 1869–1882.

Su, L.K. & Dahm, W.J.A. (1996) Scalar imaging velocimetry measurements of the velocity gradient tensor field at the dissipative scales of turbulent flows. Part II: Experimental results; Physics of Fluids Vol. 8 (7), 1883–1906.

Dahm, W.J.A., Tryggvason, G. & Zhuang, M.M. (1996) Integral method solution of time-dependent strained diffusion-reaction equations with multi-step kinetics; SIAM Journal on Applied Mathematics, Vol. 56, No. 4, 1039–1059.

Frederiksen, R.D., Dahm, W.J.A. & Dowling, D.R. (1996) Experimental assessment of fractal scale similarity in turbulent flows. Part I: One-dimensional intersections; Journal of Fluid Mechanics, Vol. 327, 35-72.

Frederiksen, R.D., Dahm, W.J.A. & Dowling, D.R. (1997) Experimental assessment of fractal scale similarity in turbulent flows. Part II: Higher-dimensional intersections and nonfractal inclusions; Journal of Fluid Mechanics, Vol. 338, 89-126.

Frederiksen, R.D., Dahm, W.J.A. & Dowling, D.R. (1997) Experimental assessment of fractal scale similarity in turbulent flows. Part III: Multifractal scaling; accepted for publication; Journal of Fluid Mechanics, Vol. 338, 127-155.

Frederiksen, R.D., Dahm, W.J.A. & Dowling, D.R. (1998) Experimental assessment of fractal scale similarity in turbulent flows. Part IV: Effects of Reynolds and Schmidt numbers; to appear in Journal of Fluid Mechanics.

Dahm, W.J.A. (1997) Fine structure characteristics of large Schmidt number molecular mixing in turbulent flows; Invited Chapter in Chemical Reactions and Physical Processes in Turbulent Liquids, (A. Gyr & F. Rys, Eds.).

Dahm, W.J.A. & Southerland, K.B. (1997) Experimental assessment of Taylor's hypothesis and its applicability to dissipation estimates in turbulent flows. Phys. Fluids 9, 2101-2107.

Dahm, W.J.A. (1998) Multidimensional scalar imaging. Invited chapter to appear in book on Flow Visualization: Techniques and Examples (L. Smits & T.T. Lim, Eds.); Imperial College Press, London.

Tacina, K.M. & Dahm, W.J.A. (1998) Effects of heat release on turbulent shear flows. Part 1. A general equivalence principle for nonbuoyant flows and its application to turbulent jet flames. Submitted to Journal of Fluid Mechanics.

Ratner, A., Donbar, J., Carter, C., Driscoll, J.F. & Dahm, W.J.A. (1998) Images of the CH and OH reaction zones of flames in the new regime of intensely wrinkled flames (in preparation).

Carter, C., Donbar, J. & Driscoll, J.F. (1998) Simultaneous CH PLIF - PIV diagnostics applied to a turbulent nonpremixed flame", to appear in Optics Lett.

Carter, C., Donbar, J. & Driscoll, J.F. (1998) Structure of the reaction zones within turbulent nonpremixed jet flames from CH-OH PLIF images, (in preparation).

Donbar, J. & Driscoll, J.F. (1998) Strain rates measured along the wrinkled flame contour of a turbulent nonpremixed jet flame, (in preparation).

## 2. Compressibility Effects on Turbulent Shear Flows

### 1. Introduction

Gaseous fuel injection and mixing with a supersonic airstream will be a key feature in future airbreathing combustion systems. Various means have been proposed for injecting fuel into a supersonic combustion ramjet propulsion system in order to achieve effective mixing and combustion. The primary challenge is to produce large mixing rates with minimal losses in a practical combustor configuration.

To help develop the necessary technical background to achieve this, AFOSR has in the past supported research efforts aimed at clarifying the fundamentals of mixing and combustion in two-dimensional turbulent shear layers. The shear layer is well suited for such studies, in part because of its fluid dynamic simplicity and the thorough documentation of its structure and dynamics under incompressible flow conditions. Numerous effects of compressibility have been seen in the shear layer studies noted above. These include changes in the similarity scaling properties of the flow (e.g. effects of compressibility on layer growth rate) as well as changes in the structure and dynamics of the large scales (e.g. two-layer structure). Many of the phenomena seen are believed to be generic compressibility effects, which will be seen in similar fashion in all turbulent shear flows.

However, some of the effects of compressibility seen in these shear layer studies are likely to result from the specific large scale structure and dynamics of that particular shear flow. Drawing conclusions about supersonic mixing and combustion from basic research studies in this flow alone may be misleading. It appears likely that flows with other fluid dynamic scaling properties, and therefore other large scale structure characteristics, will demonstrate some of the effects of compressibility seen in shear layers, and will show also certain new effects not seen in shear layers.

Aside from these changes in the large scale structure due to compressibility, it appears likely that there are changes in the small scale structure as well. Classical scaling laws that relate the inner (small) scales of turbulent shear flows to the outer (large) scales rely on a balance in the energy transfer process between these scales. When shock waves and expansion waves are present, there are known to be changes in the energy transfer process that can potentially lead to an alteration of inner-outer scale ratio, and possibly even to fundamental changes in the physical structure of the small scales themselves. Moreover, in the presence of heat release values typical of hydrogen or hydrocarbon fuels, the associated

volumetric expansion near the reaction zones can potentially lead to further changes in the small scale hydrodynamics with attendant changes in the scalar mixing process at the small scales. Identifying these effects of compressibility requires high resolution measurements of the small scales, and comparisons with similar results obtained for the small scale structure in incompressible turbulent shear flows.

This part of our study has as its aim to compare results obtained to date for mixing and combustion in compressible turbulent shear layers with new measurements in supersonic coflowing turbulent jets. There have been a number of previous studies of supersonic combustion in turbulent jet flows; e.g. Crookson et al (1969); Slutsky et al (1965); Drewry et al (1972); Northam et al (1989). However, many of these have involved complications in both the geometry and the flow characteristics that prohibit detailed comparisons with shear layer results, and have been limited in the measurements obtained. The present study is among the first opportunities to obtain detailed measurements in a compressible turbulent shear flow (other that the mixing layer studies mentioned above) that has been intentionally designed to permit careful study of the large-scale and small-scale flow properties under reacting and nonreacting flow conditions. The results obtained have allowed comparison with comparably careful experiments in turbulent shear layers to identify generic effects of compressibility on the structure and dynamics of turbulent shear flows.

## 2. Facility

Results were obtained in a novel, high-quality, flow facility has been designed and assembled at Michigan for supersonic combustion studies in coflowing turbulent jets. This facility, outfitted with a suite of advanced laser diagnostics that allows planar laser induced fluorescence (PLIF) access to CH and OH, in addition to conventional high-quality schlieren and shadowgraph imagery, is shown in Figs. 1 and 2.

Primary components and capabilities include a Supersonic Combustion Section designed for Mach 2.2 air flow with stagnation temperatures up to 600K and nominal test section stagnation pressure of 6.44 atm. The combustion section is 55 cm long and nominally 5.77 cm × 4.06 cm in cross section, and has two-dimensional, parallel sidewalls for optical access, with wall divergence angles adjustable from 0–6° to eliminate thermal choking. A total of 30 static pressure taps and pitot probe ports are located on the test section walls to monitor the wall static pressure distribution and test section Mach number distribution. Access for advanced optical diagnostics is provided by 8 Vycor glass

windows. A settling chamber immediately upstream of the two-dimensional supersonic nozzle contains a 42% blockage perforated plate and quieting section for inflow turbulence control. The facility also includes a 250 kW Electric Air Heater, with a length 5.3 m, capable of heating up to 1.0 kg/sec air flow to temperatures as high as 1100K. A digital control circuit maintains constant stagnation temperature to within ±0.5K in the settling section. Electric heating was chosen over a vitiated air design to avoid radicals present in variable concentrations in a vitiated air system, which are known to affect combustion stability.

The facility also has a Diffuser and Exhaust Duct Section located at the exit of the supersonic test section. The water-cooled diffuser section has a constant area of 5.1 cm × 11.9 cm and is 78.7 cm long, and is outfitted with 5 static pressure taps and two 1.3 cm × 29 cm Vycor glass windows. The exhaust duct section has a circular cross-section, 10.8 cm in diameter, with two sampling probe ports located 125 cm and 240 cm from the supersonic test section entrance.

The test section can be fitted with an Axisymmetric Fuel Injection Tube or a Two-Dimensional Slot Nozzle. The axisymmetric fuel injection tube was located 16.5 cm downstream of the test section inlet. Gaseous hydrogen fuel is injected at speeds up to the sonic velocity of hydrogen (1190 m/sec at 294K stagnation temperature) to form a supersonic coflowing turbulent jet in the test section. Six ignition ports are located near the test section entrance. The fuel tube has an inner diameter of 0.70 cm, and can be fitted with four different bluff body tips, having outer diameters ranging from 0.84 cm to 2.54 cm, to create recirculation zones of varying size. The resulting primary reaction zone length is typically 40 cm long. The two-dimensional slot nozzle had a 2 mm inside width and wall thickness of 1.1 mm.

## 3. Diagnostics

Advanced laser diagnostics, including acetone PLIF for mixing studies, PLIF access to CH and OH species concentration fields, and conventional high-quality schlieren and shadowgraph imagery have been used in various parts of this study. Figure 3 shows a schematic of the laser diagnostic set-up used on the supersonic combustion tunnel for studies of entrainment and mixing in the supersonic coflowing turbulent jet. Results from these laser diagnostics are presented in later sections of this report.

Planar laser Mie scattering (PLMS) images were also used to document the growth rate of

the jet under nonburning conditions. In this case, alcohol vapor was created by spraying ethanol approximately 1 m upstream of the nozzle. The mass fraction of alcohol in the fuel stream is approximately 1%. Alcohol vapor is condensed due to mixing of the fuel stream with the cold, supersonic ambient stream and forms a fine fog from which light is Mie scattered.

Schlieren photographs of the wave patterns that result in the test section, when fitted with the two-dimensional slot nozzle, are shown in Fig. 4. These photographs demonstrate the wave patterns at various fuel delivery pressures, corresponding to increasing values of the jet momentum flux per unit span. For supersonic combustion studies with the axisymmetric fuel injection tube, the thermal choking phenomenon varies with wall divergence angles. In practice, wall divergence angle is set to avoid choking and maintain constant Mach number within the test section. Measurements have also been made to verify the flow quality in the supersonic test section, both for cold flow testing, as well as for flows under supersonic combustion conditions.

## 4. Results

Figure 5 shows typical results from the PLMS imaging studies of the supersonic coflowing jet at three separate instants of time. Note the large scale structure of the flow in the downstream portions of each image. In the planar turbulent jet (or wake), the structures form into a staggered array of vortices with alternating signs of circulation. It is also apparent that there is little or no evidence of such structures for some distance beyond the jet exit.

Figure 6 shows a typical instantaneous PLMS image and the average image to allow comnparison between the two. Note the growth rate $d\delta(x)/dx$ of the jet in the average field. This growth rate, in part, sets the entrainment and mixing rates of the flow, and was measured in this study.

The mean scalar profiles obtained from the average PLMS image are shown at various downstream locations in Fig. 7, together with typical wall pressure measurements. These scalar profiles were then used to determine $\delta(x)$, where the outer length scale $\delta$ was defined both by the full width at the 5% points of the Gaussian fit to each individual profile, and from the half-width $\delta_{1/2}$ at which the mean scalar values have dropped to half the centerline value.

Results for the variation in outer length scale $\delta(x)$ are shown, for both definitions, in Fig. 8. Note that the results are presented in linear, as well as logarithmic, axes to allow power-law scaling to be identified. In the log-log forms, it is evident that power-law scaling is found in the downstream portion of the flow, as indicated by the straight line on which the data fall. The slope of this line gives the exponent in the power-law scaling and is found to match the $x^{1/2}$-scaling characteristics of the wake-like limit of incompressible coflowing turbulent jets.

The downstream region over which the $x^{1/2}$-scaling is found agrees well with the range of x over which clear evidence for quasi-periodic large-scale structure is found in the flow. These results together suggest that, where the convective Mach number is believed to have decreased to sufficiently low subsonic values, the power-law scaling of the flow, its large-scale structure, and its entrainment and mixing rates, have returned to their original incompressible values.

These conclusions are further supported in Fig. 9, where the power-law scaling of the flow, as measured both by the mean scalar profiles of the type in Figs. 6 and 7 and by the mean velocity profile determined from pitot probe measurements, is compared with the classical result from studies of incompressible turbulent wakes. The results show that, except for an offset that appears to be due to the effect of the near field in which the convective Mach number is supersonic, the results follow the incompressible scaling. Current work is focusing on the near field and on experimental studies of the structure and scaling of the flow in that part of the flow where the convective Mach number is supersonic.

The impact of the results is considerable. Progress in developing effective combustion sections for scramjet propulsion systems relies in part on results being obtained from fundamental studies of supersonic mixing and combustion in turbulent shear flows. Conclusions drawn from studies such as this, together with earlier results from turbulent mixing layers, are identifying those effects that are genuinely applicable to compressibility in all turbulent flows and those that are specific to the structure and scaling properties of the classical turbulent mixing layer. Moreover, these supersonic coflowing turbulent jet combustion studies are greatly contributing to the base of data available from carefully designed experimental facilities on compressibility effects in turbulent flows.

# Supersonic Combustion Tunnel Facility
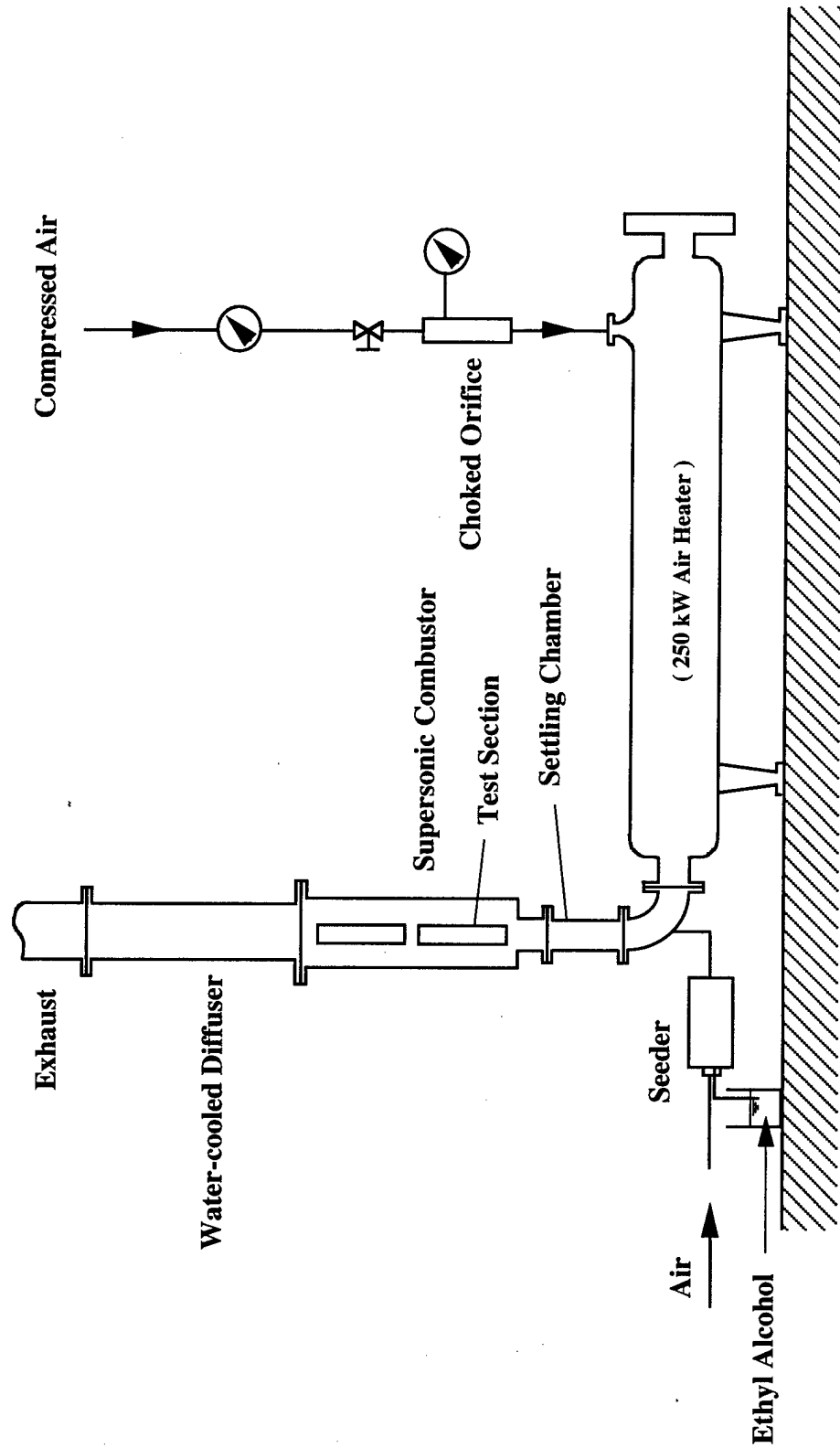


Figure 1. Schematic of the major components of the Michigan Supersonic Combustion Tunnel.
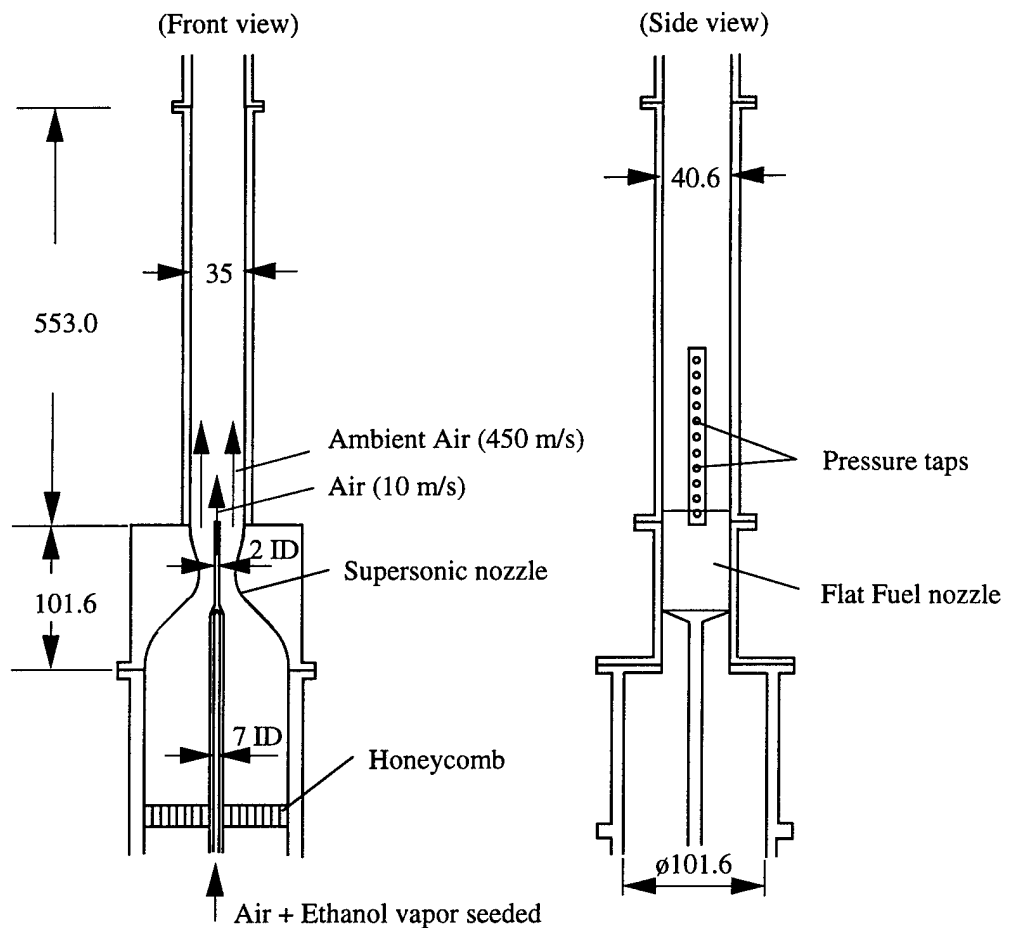
Figure 2. Schematic diagram of the test section (unit: mm)
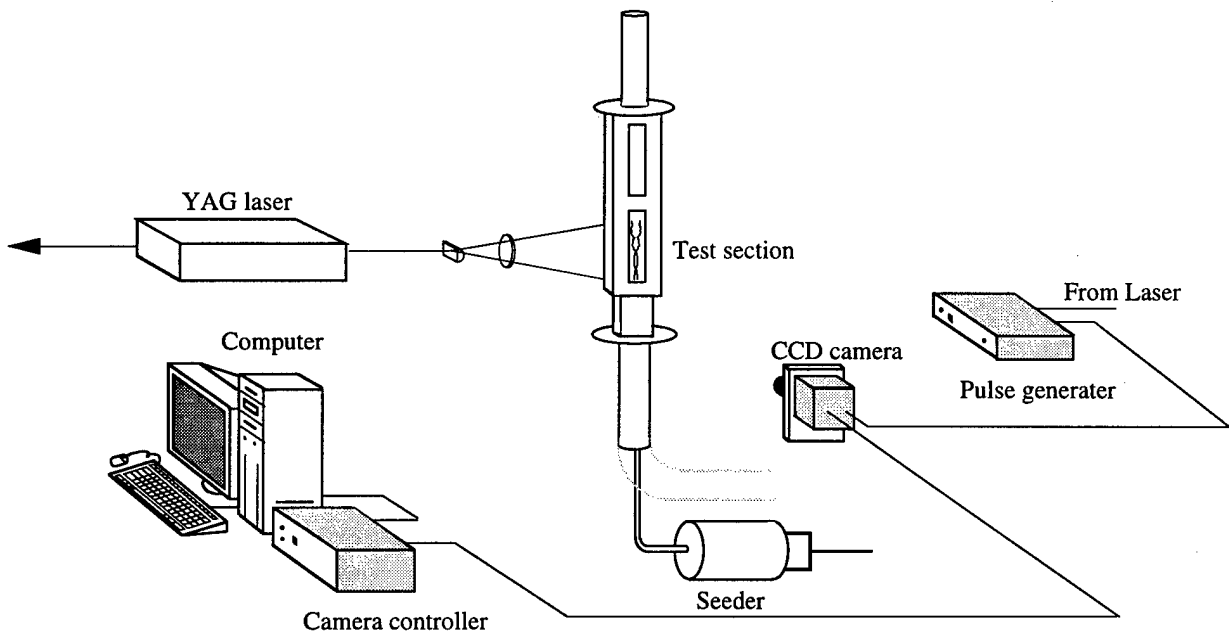


Figure 3. Schematic diagram of the imaging system
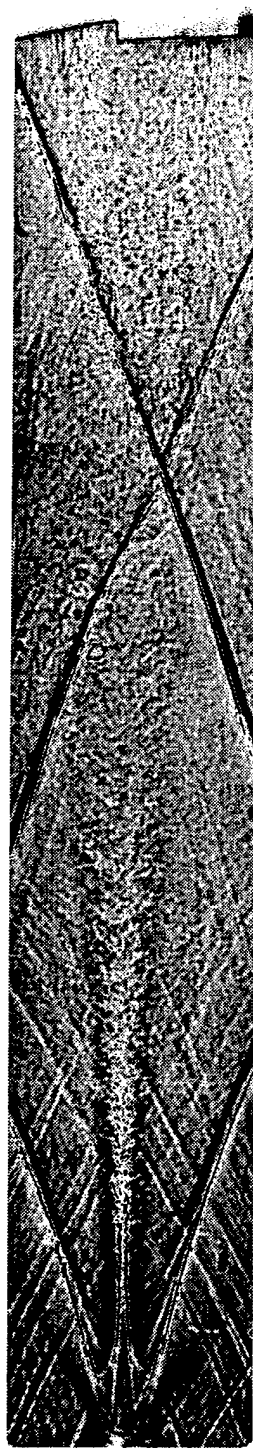
**30 psig**
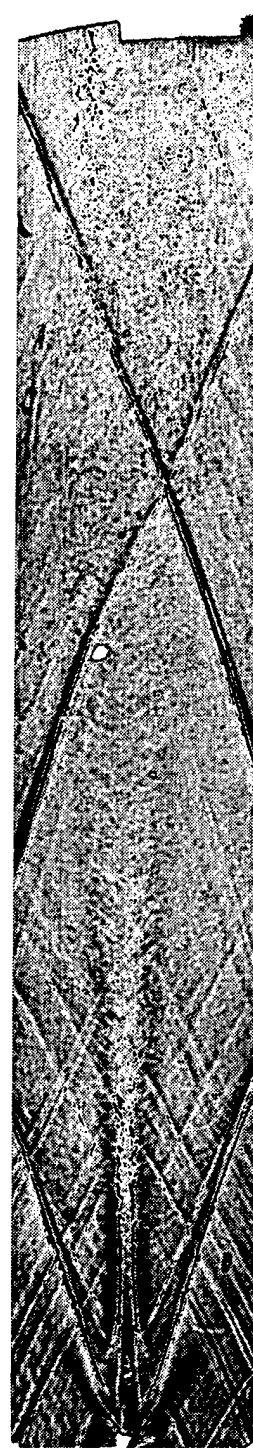
**45 psig**
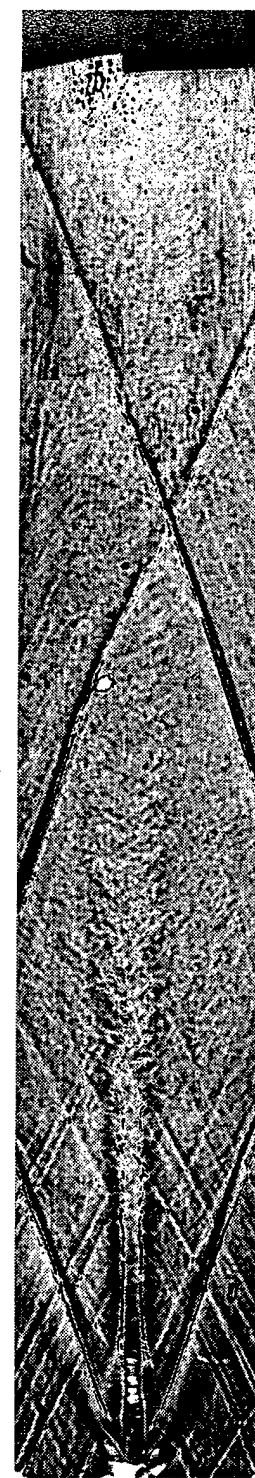
**60 psig**

Figure 4  Schlieren images of the propane jet (wake) and wave pattern in the test section at various fuel pressures.
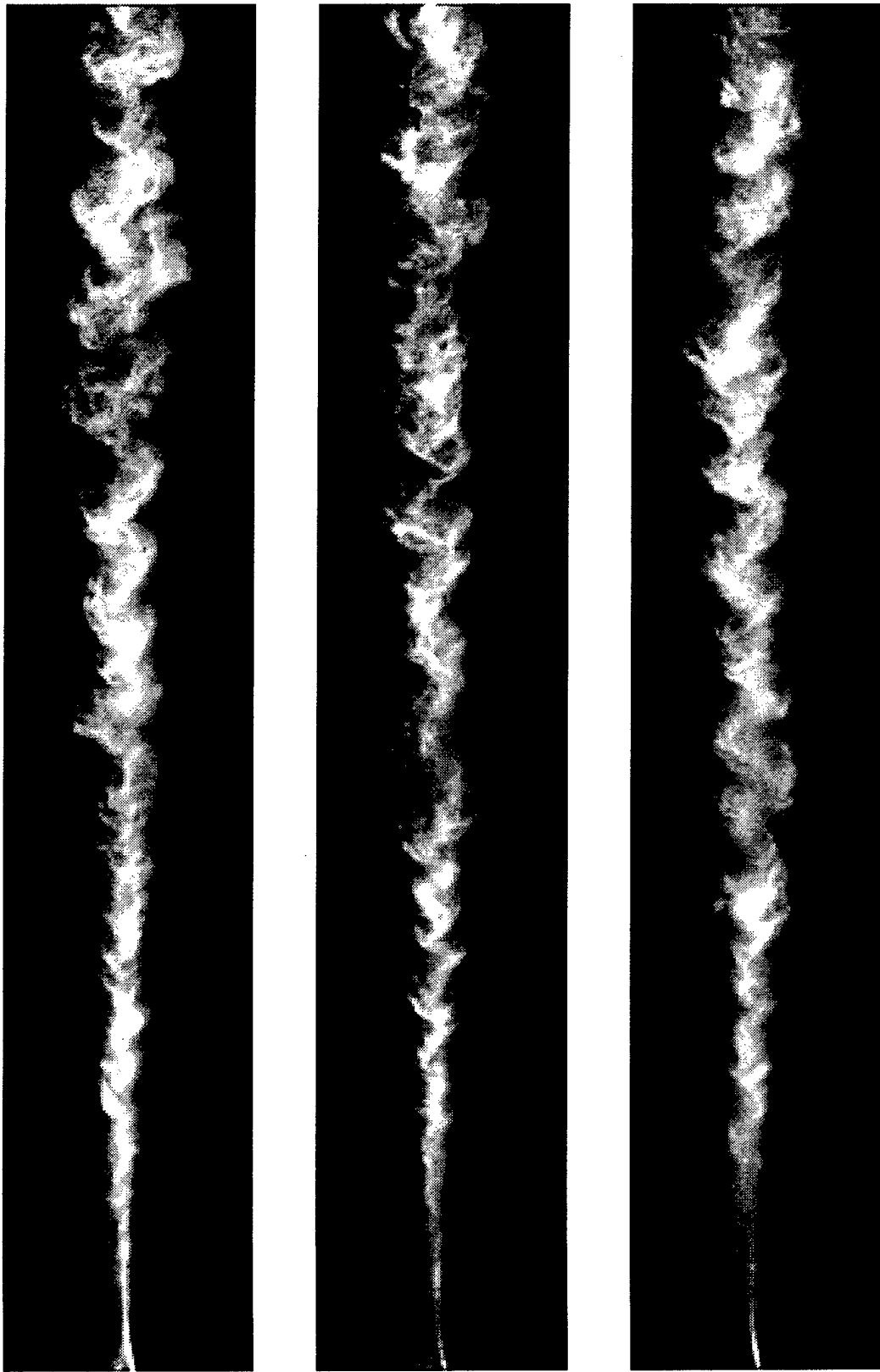
Fig. 5. Typical large-scale structure in the two-dimensional supersonic turbulent shear flow shown in three different realizations, visualized by alcohol fog technique. Note the large-scale structure is clearly evident in the farther downstream regions of the flow, where the local Mach number is subsonic.

11
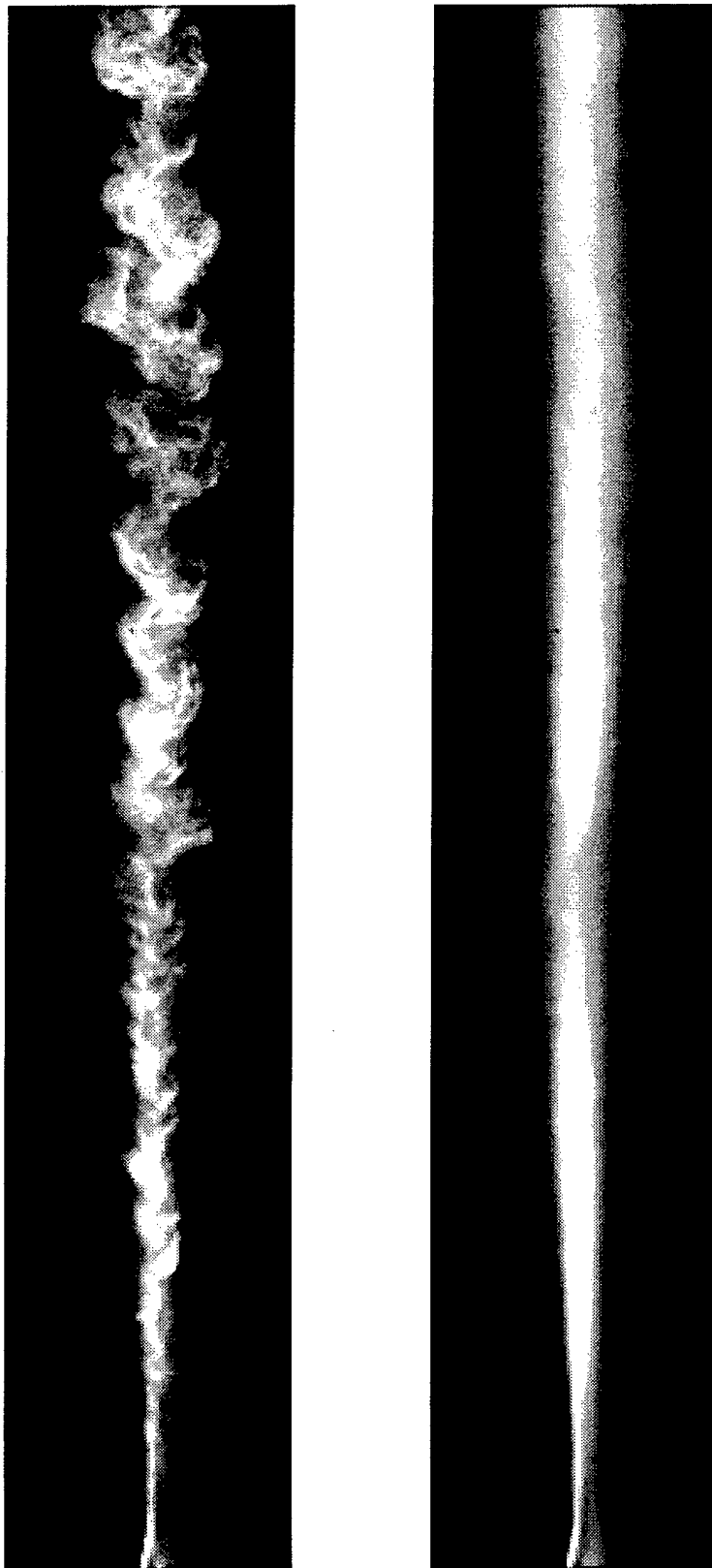
Figure 6. Comparison of instantaneous (top) and average (bottom) scalar field images as visualized by the PLMS technique. Note the large scale structure evident in the downstream portions of the instantaneous image. No structure is evident in the upstream portion of the instantaneous image. Dark zones in the mean image are due to interactions with oblique shock waves.
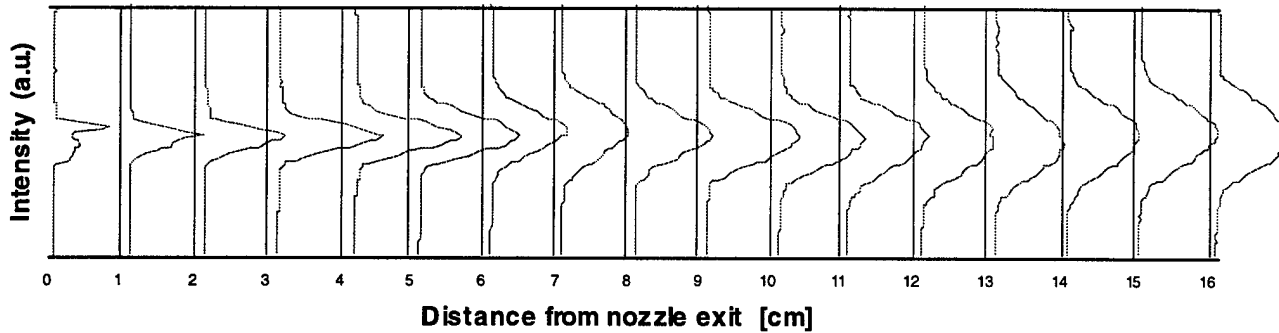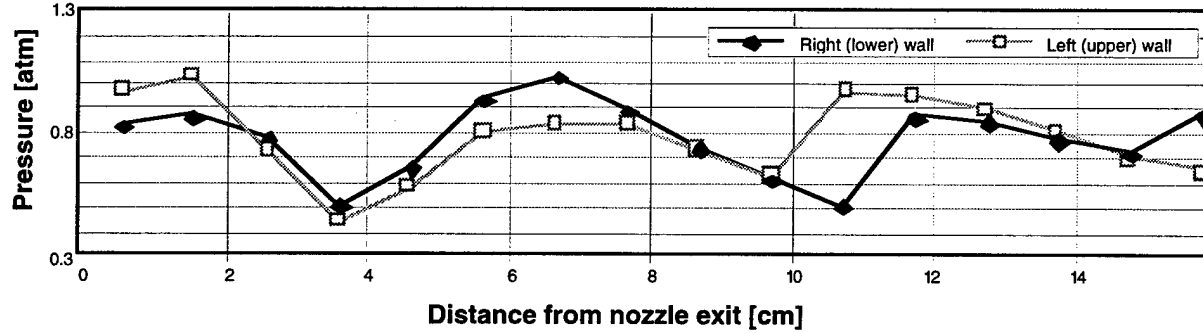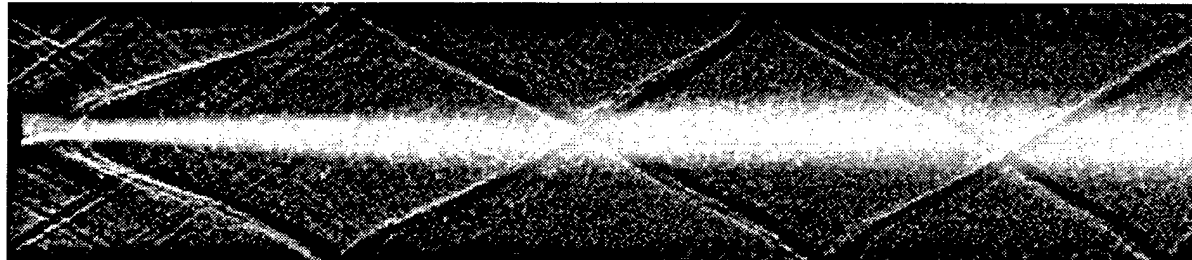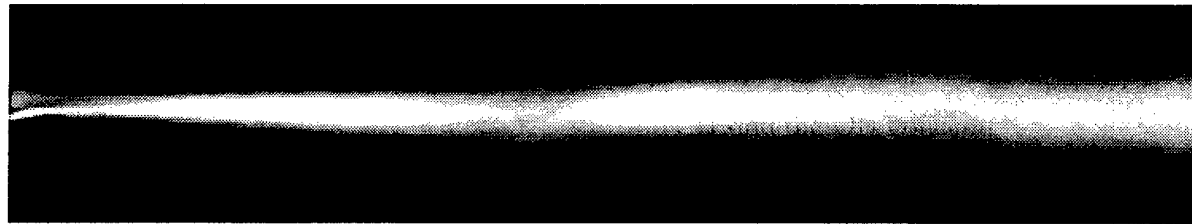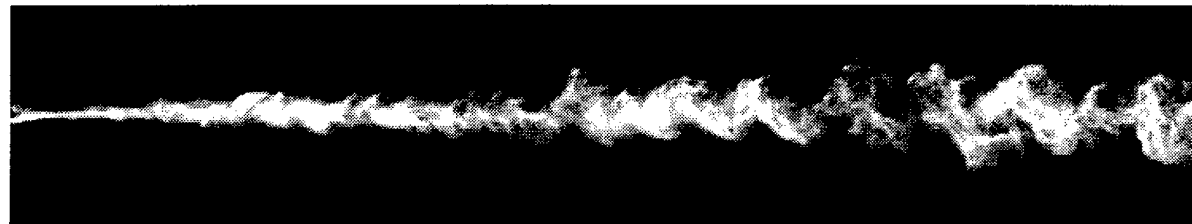
Fig. 7. Typical experimental results for outer-scale properties obtained in the two-dimensional supersonic turbulent shear flow, showing instantaneous mixing regions and large-scale structure as visualized by alcohol fog technique *(top)*, ensemble average *(second)*, with supersonic wave structure superimposed *(third)*, wall static pressure measurements *(fourth)*, and local flow width d(x) as indicated from second panel. See also Figs. 5 and 6. Growth rates obtained from bottom panel are shown in Fig. 8.

13
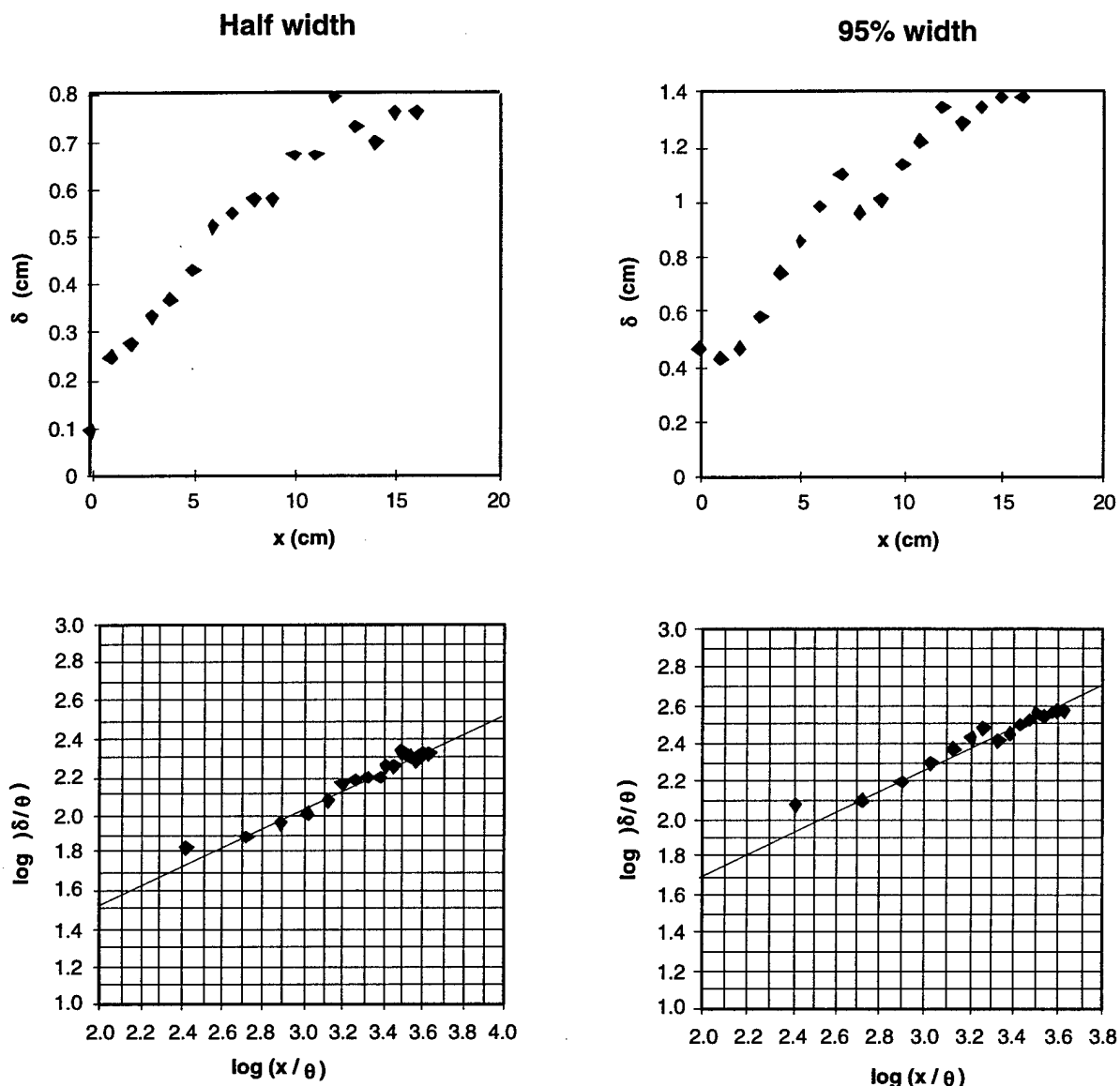
## Half width

## 95% width



Figure. 8.   Measured variation in local outer-scale flow width  δ(x) defined by half-width *(left)* and 95%
width *(right)* with downstream distance x/ θ in the two-dimensional supersonic shear flow,
shown in linear form *(top)* and logarithmix form *(bottom)*.  Note straight line gives $(x/ \vartheta)^{1/2}$
power law scaling.

14
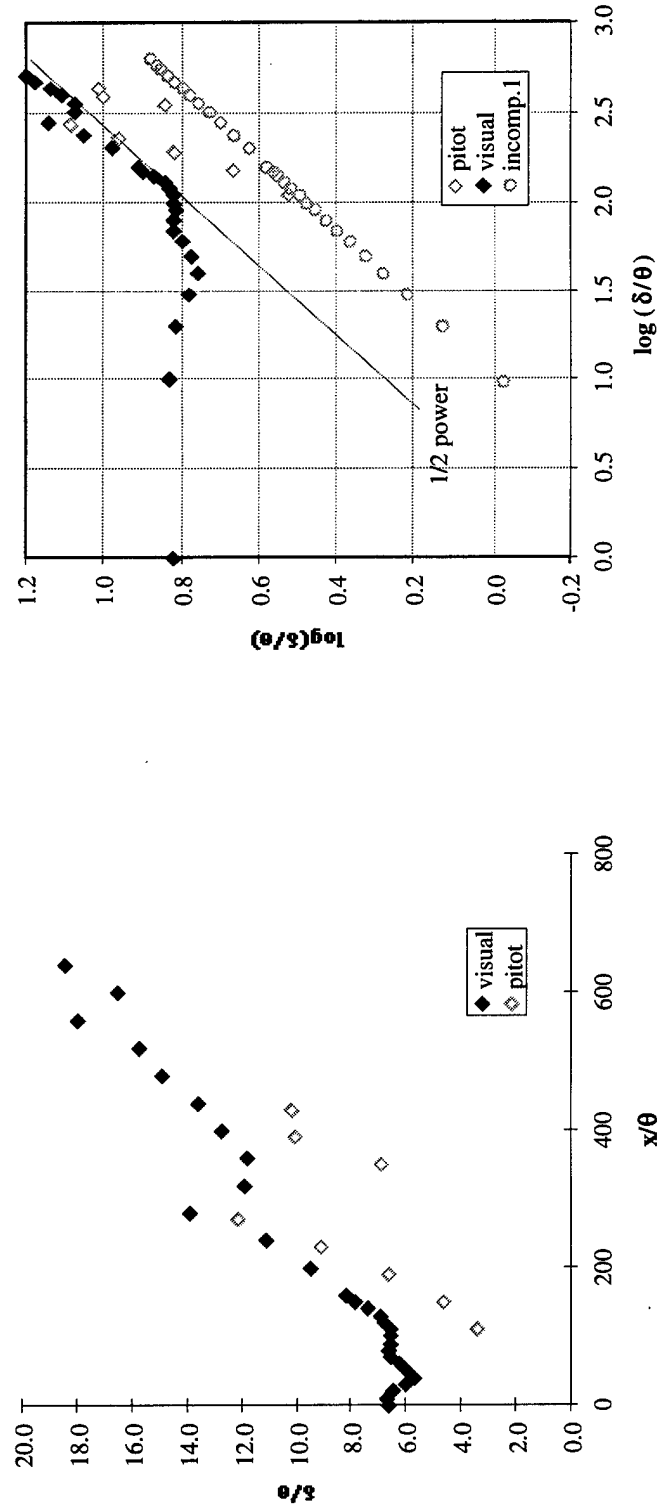
Figure 9. The measured growth rate $\delta/\vartheta$ vs. $x/\vartheta$ obtained from the mean scalar profiles in Fig. 7 and from pitot probe measurements, shown in linear scale (*left*) and log-scale (*right*).

15

## 3. Supersonic Turbulent Combustion

Early results (e.g. Fig. 10) indicated that strong interactions occurred between waves in supersonic flows and the entrainment, mixing, and combustion processes. Experimental studies were therefore conducted to determine fundamental phenomena associated with supersonic turbulent combustion. Some of the first images of fuel concentrations and the reaction zones within supersonic flames were obtained using acetone and OH PLIF diagnostics. Trace amounts of acetone were added to the hydrogen fuel, which was injected at Mach one along the axis of a supersonic wind tunnel; the Mach number of the surrounding air is 2.5.

The OH PLIF images show that the structure of the supersonic flame is different from that of a subsonic flame; e.g. see Figure 11. The differences appear to simply be due to the larger velocity differences in high speed case and are not due to compressibility effects. In the supersonic case, even a small lifting of the flame causes large amounts of air to be entrained into the fuel before combustion occurs. The supersonic flame therefore has properties of a partially premixed flame, while the corresponding subsonic flame, for the same liftoff height, has properties of a diffusion flame. In the supersonic case, the large air velocity creates a strong recirculation zone which entrains air into the liftoff region. The OH PLIF images for the supersonic flame show that OH exists in a homogeneous, broad region near centerline, which is similar to the OH pattern behind a premixed V shaped flame. In contrast, the subsonic flame has no homogeneous OH zone but is made up of many thin flamelets of OH, which are entangled. At lower speeds there is no OH near centerline except at the flame tip, which is a completely different from the supersonic case.

It is concluded that, since all supersonic flames are slightly lifted and thus will become partially premixed, as seen herein, conventional diffusion flame models should not be adequate to model supersonic flames. Instead, modifications will be required to account for partial premixing. Without such modifications, the prediction of fundamental quantities such as supersonic flame length and heat release pattern cannot be expected to be accurate.

The work shows that images of the reaction zone are necessary to understand supersonic flames and that OH and acetone PLIF diagnostics can be successfully used in supersonic flames. It is planned to use CH PLIF imaging to study the fuel decomposition zone of supersonic hydrocarbon - air flames.

THERMAL
CHOKING

$\dot{m}_F$ = 1.6 g/s
10° wedge

$\dot{m}_F$ = 1.0 g/s
15° wedge
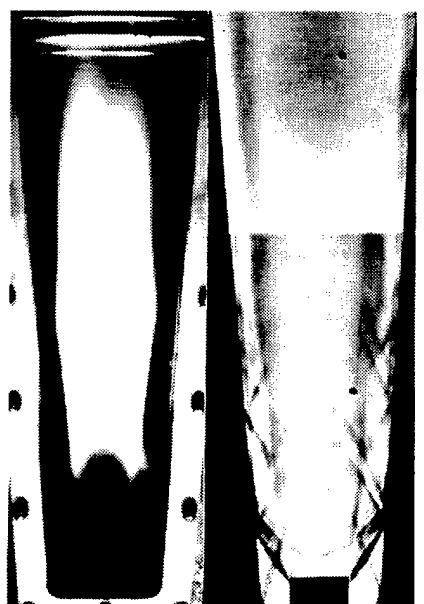
$\dot{m}_F$ = 1.6 g/s
no wedge

NO COMBUSTION

no wedge       10° wedge

Figure 10. Direct and schlieren photographs of supersonic jet-like flames with and without interacting shock waves. Hydrogen mass flowrate is varied from 0.4 to 1.4 g/s. Shock waves generated by wedges on the sidewalls interact with the flow to produce significant effects on the reacting flows. Window height is 30.5 cm (12 in.), and distances in the schlieren images are 20% larger than in the direct images. From Huh (1996).

17
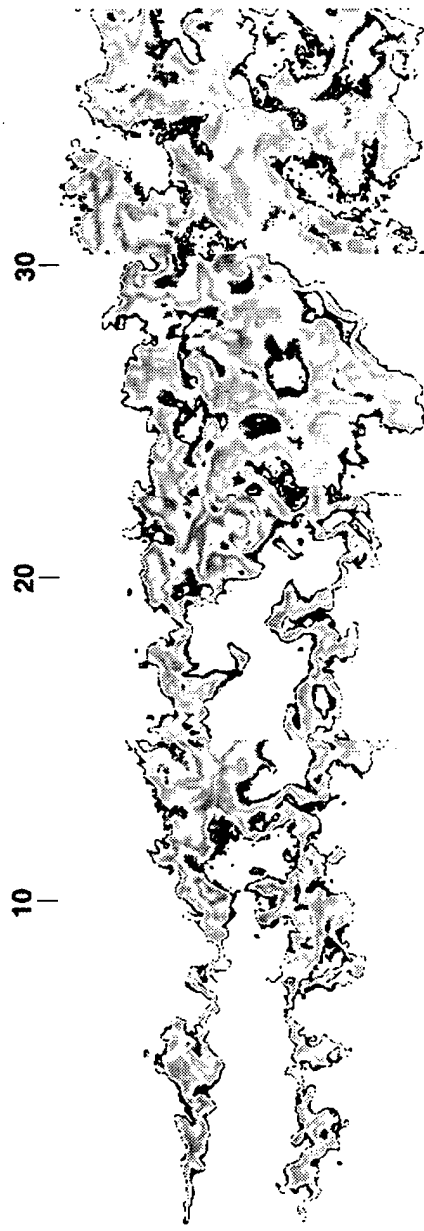
**Subsonic Flame OH PLIF Image**
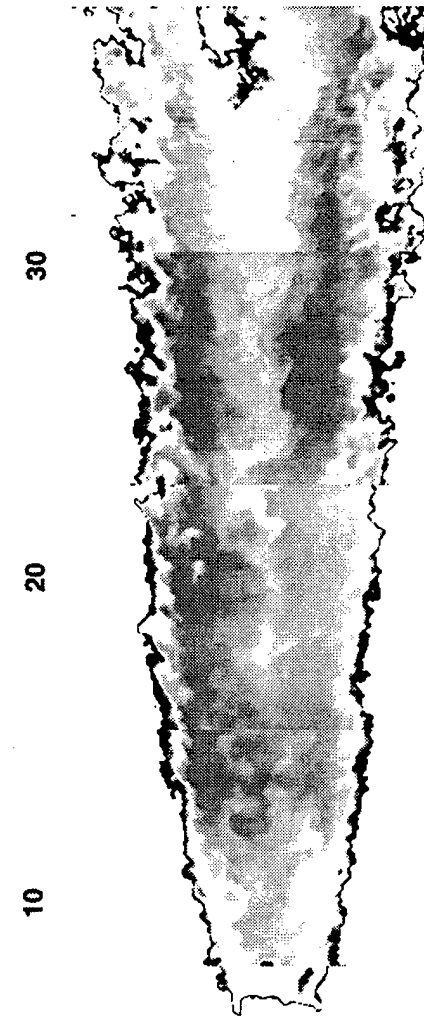
**Supersonic Flame OH PLIF Image**

Figure 11. Comparison of OH PLIF imaging measurements showing flame structure in subsonic (*top*) and supersonic (*bottom*). Note the very different structure under supersonic flow conditions.

## 4.  CO / OH PLIF Imaging of Turbulent Nonpremixed Flames.

Simultaneous CH/OH imaging measurements were conducted to study various aspects of turbulent flame structure, with sample results shown in figures 12-15.  Parts of this work were done through an  interaction with the Air Force Research Laboratory Propulsion Directorate, Wright-Patterson Air Force Base (Dr. Tom Jackson).

Results have shown that simultaneous images of the CH and the OH concentration fields can be obtained throughout a high Reynolds number (18,600) turbulent nonpremixed jet flame (even near the flame tip) and that the CH-OH boundary is a useful marker of the location of the stoichiometric flame contour.  The structure of the fuel decomposition reaction zone is identified by the CH images, including:  high curvature cusp regions, CH extinction regions, and the "splitting" of the flame due to oxidizer entrainment to the centerline.

It was found that the fuel decomposition reaction zone layer remains thin and rarely exceeds 1 mm, even near the tip of the high Reynolds number flame.  Turbulence does not significantly broaden the fuel decomposition reaction zone, since CH layers in the turbulent flame are not more than 25% thicker than CH layers that were measured in a laminar jet flame. The mean thickness of the CH reaction layer increases from 0.3 to 0.8  mm in the streamwise direction, which is expected because scalar gradients (and dissipation rate) are predicted to decrease in the streamwise direction. The flame surface density is measured to be typically 0.2  $mm^{-1}$, and is shown to be related to the turbulent brush thickness and the degree of wrinkling.   It was shown that a "permanently blue" turbulent jet flame could be achieved using the nitrogen-diluted fuel suggested by the laminar studies of Du and Axelbaum, which allowed CH to be imaged throughout the flame.

It is demonstrated that the CH-OH boundary can be measured at all locations within a turbulent jet flame; this boundary is an unambiguous marker of the instantaneous stoichiometric contour.  The presence of CH is proof that the flame exists at a particular location.

The reaction zone structure in the jet flame is characterized by regions of large flame curvature (cusps), and a "splitting" of the flame into separate sections and pockets (in the measurement plane) due to the entrainment of oxidizer to the centerline.  Turbulence does not significantly broaden the reaction zone that is associated with the fuel decomposition reactions which involve CH, even near the tip the high Reynolds number (18,600) flame.  CH layers remain thin  (less than 1 mm thick) and are nearly equal in thickness to the CH layers measured in a laminar jet flame at the same x/d location.  However, the thick OH structures that were observed are in agreement with previous OH structures imaged by Seitzmann et al and Starner et al; turbulence causes the

OH zones to be broader than those in the laminar jet flame. It cannot be determined if the thick OH zones are simply due to hot water vapor in the post-flame gases or if heat release occurs in these OH zones.

The thickness of the CH layer is found to increase in the downstream direction, which is consistent with theory that predicts that the layer thickness scales inversely with the square root of the scalar dissipation rate. The flame surface density was measured, and the peak value of S on each radial profile decreased in the axial direction as the flame brush increased. This trend is consistent with a physical description of S that is presented, which indicates that S should scale inversely with the flame brush thickness. Typical values of S were found to be 0.2 to 0.3 $mm^{-1}$.

The OH boundary alone is a less definitive marker of the flame than the CH-OH interface; the presence of an OH boundary does not insure that a flame exists at that location. It may not be clear if a particular OH boundary is the stoichiometric boundary or is an interface with the entrained air.

It was demonstrated that CH PLIF and PIV diagnostics can be used simultaneously to first identify the wrinkled flame contour within a high Reynolds number turbulent nonpremixed jet flame and then to measure the local strain rate on this surface. An understanding of the strain rate (and the corresponding stretch rate) is needed to *(a)* explain and model the flame surface density (S) and turbulent reaction rate (wF), *(b)* determine if strain rates scale with the ratio of jet centerline mean velocity to jet width, and *(c)* assess the validity of flamelet assumptions. A significant fraction (42%), but not all, of the strain could be measured; the out-of-plane contribution should be nearly equal to the measured values for all conditions and thus should not change any of the conclusions. The estimated 16% contribution due to the small unresolved eddies also should not affect the trends observed.

It is found that the measured strain rates on the flame surface do not scale with the ratio of centerline velocity to jet width, which is proportional to $U_F d/x^2$, where $U_F$ is the fuel exit velocity, d is the exit diameter, and x is the downstream distance. Surprisingly, the strain rates do not decrease in the streamwise direction because of the geometric alignment of the flame surface. In the base region the flame is usually parallel to the velocity vectors, causing negative stretch contributions, whereas near the flame tip the wrinkled flame is often perpendicular to the velocity vectors, leading to large extensional strain (and positive stretch). Strain also is found to have a stronger dependence on the fuel velocity ($U_F$) than the theory predicts.

It was demonstrated that CH PLIF/PIV diagnostics can be used simultaneously in order to identify the thin CH reaction zone layers and to quantify the strain rate on these layers within a turbulent jet

flame. Large values of strain rate were measured which exceed 10,000 $s^{-1}$; the large strain rates do not occur where the flame remains vertical but occur where the flame is wrinkled by the largest vortices. Measured mean strain rates on the flame contour do not agree with the predicted $(U_F d/x^2)$ scaling relation; mean strain rate is constant in the streamwise direction and increases more rapidly with jet velocity than predicted. It is suggested that a flame wrinkling factor be added to the theory, which is found to vary as the square of the jet Reynolds number. The various components of the strain rate also were quantified; the shear term dominates over the axial term and radial terms.

The conditionally averaged mean axial velocity at the flame sheet was found to be remain constant from the base to the tip and did agree with the theoretical prediction. The out-of-plane strain rate was estimated to be nearly equal to the measured in-plane values, based on measurements of the components of the normal to the flame and the assumptions of isotropic velocity gradients. The small scale contribution was estimated to be approximately 16% of the measured values, based on an extrapolation of data obtained with different spatial resolution.

**OH PLIF**  **CH PLIF**
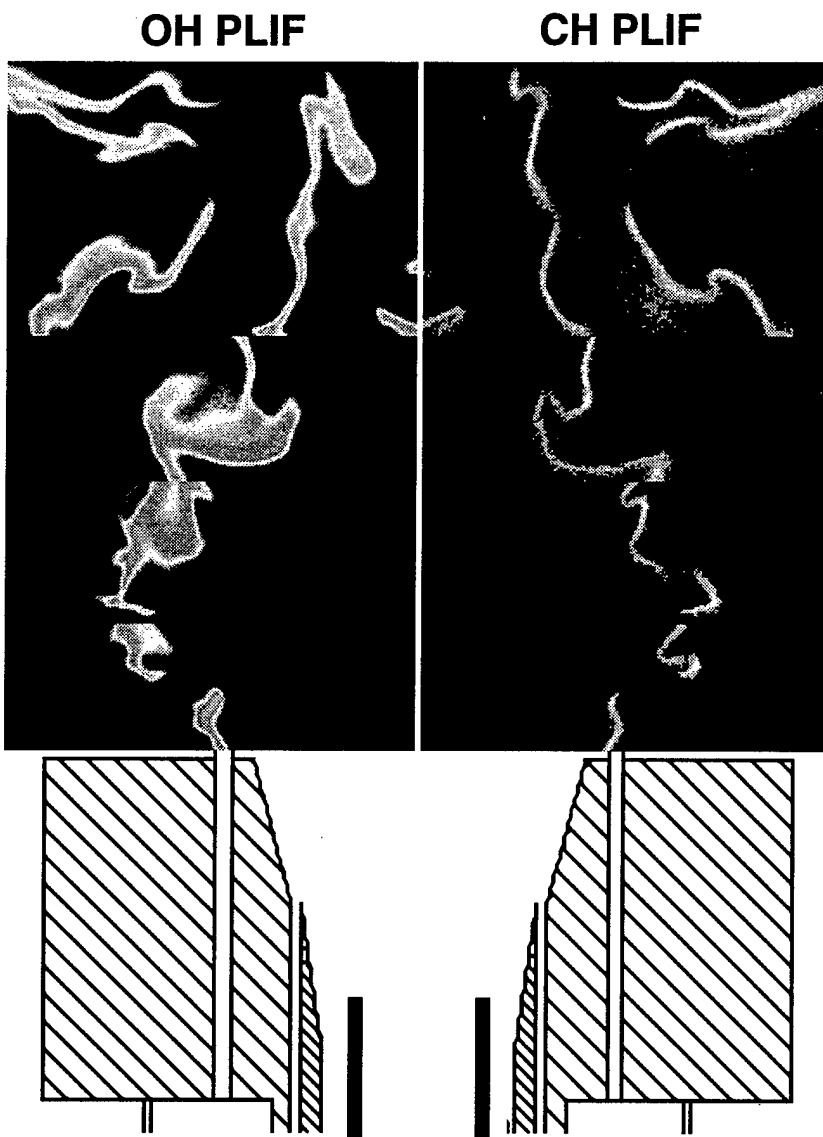
Figure 12. Typical composite simultaneous CH/OH PLIF imaging measurement of the flame structure in a swirl-stabilized combustor configuration, in which fuel issues from a tube on the centerline and forms a classical diffusion flame. The CH PLIF marks the relatively thin flame sheet in which essentially all the combustion occurs., consistent with the OH PLIF image. A second example is shown in figure 13. These should be compared with the flame structure seen in figures 14 and 15 when the fuel injector is slightly altered.

22

**OH PLIF**          **CH PLIF**

Figure 13. Another typical example of the composite simultaneous CH/OH PLIF flame structure in a swirl-stabilized combustor configuration of the type in figure 12. Note the relatively thin and closed flame sheet near the periphery of the recirculation zone. Compare with the flame structure seen in figures 14 and 15 when the fuel injector is slightly altered.

**OH PLIF**     **CH PLIF**
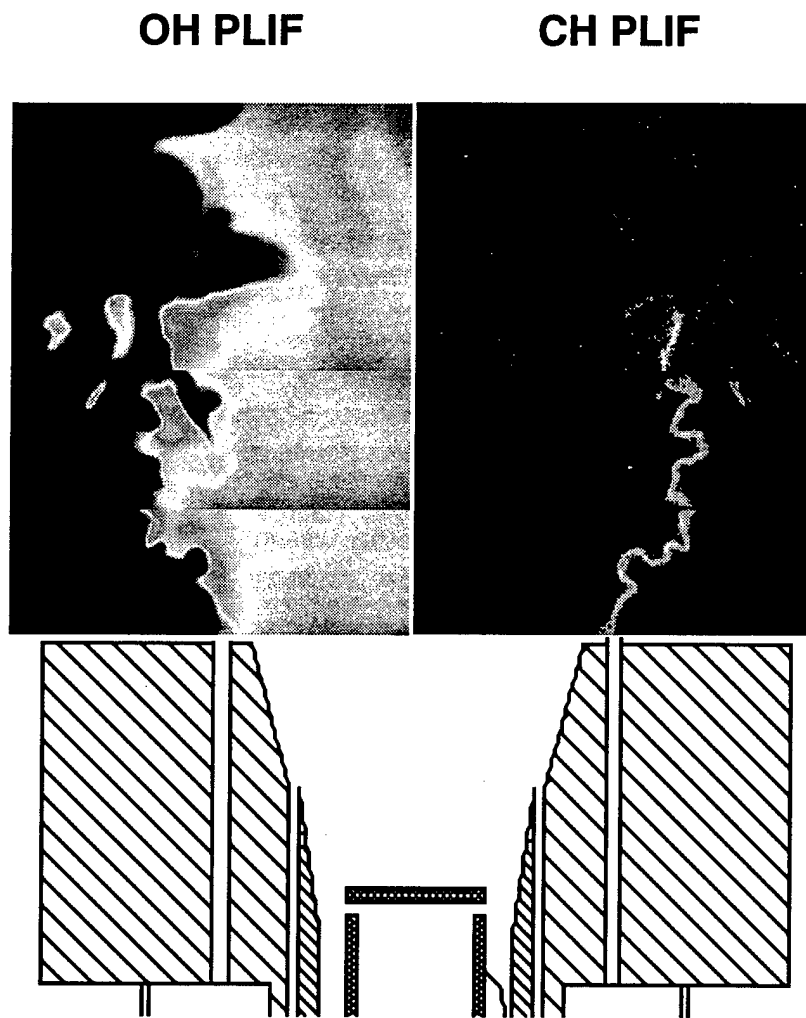
Figure 14. Typical composite simultaneous CH/OH PLIF imaging measurement of the flame structure in a swirl-stabilized combustor configuration, in which fuel issues radially outward from a tube on the centerline. The combustor and operating conditions are identical to those in figures 12 and 13 except for the radial fuel injection. In this case theCh field is consistently open, and the OH field indicates a hot core in the recirculation zone that is not seen in figures 12 and 13.

**OH PLIF**  **CH PLIF**
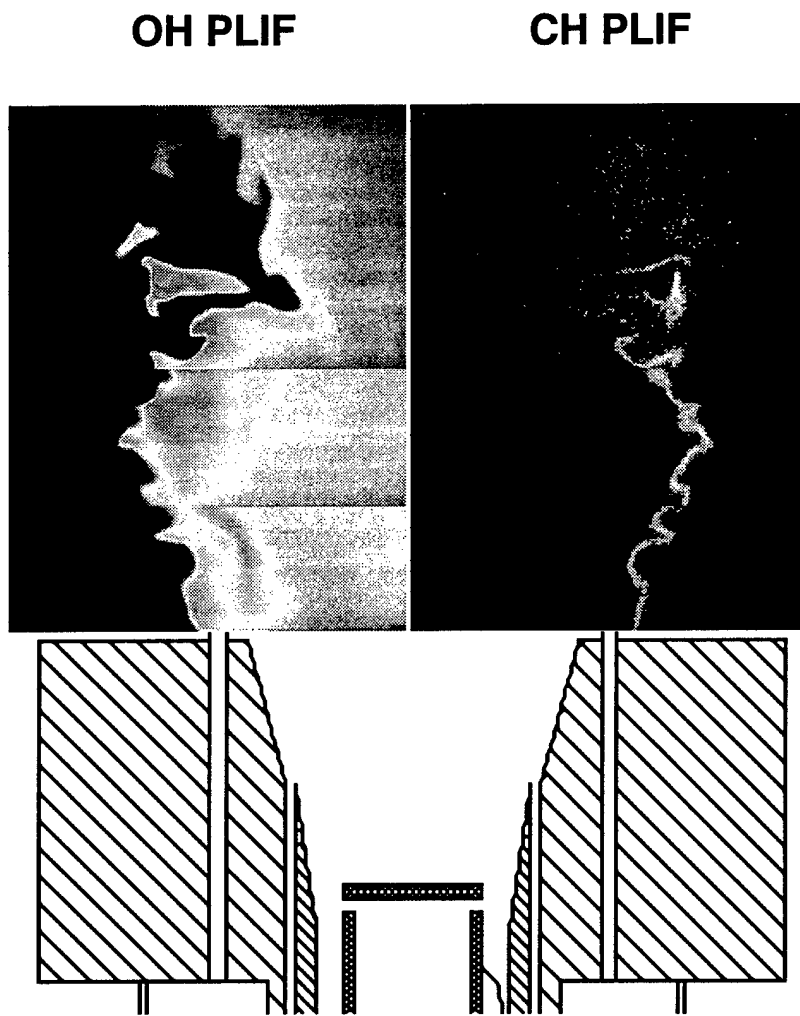


Figure 15. Another example of the typical composite simultaneous CH/OH PLIF imaging measurement of the flame structure for the swirl-stabilized combustor configuration, in figure 14. Despite the relatively small change in the fuel injection, the resulting CH and OH fields show a remarkably different flame structure. These results suggest that many results as to flame structure obtained from traditional laboratory flames may not carry directly over to more complex fuel injection geometries.

# 5. Heat Release Effects on Turbulent Shear Flows.

## 5.1. Introduction

Proper accounting for the effects of reaction heat release on the properties of turbulent shear flows is an essential bridge between fluid dynamics and combustion science. Studies of mixing without heat release in jets and other shear flows, for instance, have been used in combustion science since the earliest studies of Hottel & Hawthorne (1949) and Hawthorne, Weddel & Hottel (1949). Yet it has been widely observed that density changes due to heat release dramatically alter some of the most fundamental properties of these flows, even under conditions for which buoyancy effects are negligible. Based on such observations, the relevance of results from flows without heat release to exothermic reacting flows has long been questioned, with some studies concluding that flows with heat release are inherently different from nonburning flows.

Though many aspects of turbulent shear flows are observed to change with combustion heat release, interest is, in practice, often focused on entrainment and mixing rates, since these processes determine such fundamental properties as flame lengths, heat release distributions, induced flow fields, and mutual interference effects. Accordingly, there have been attempts to heuristically account for changes due to heat release on the entrainment and mixing properties of some specific flows, but to date no fundamentally rooted and generally applicable approach exists to predict the effect of heat release on turbulent shear flows.

There are, of course, many elementary phenomena that can occur in a flow as a consequence of heat release. These include changes in fluid viscosity, which can increase dramatically with temperature and thereby lead, in part, to a large reduction in Reynolds number. However in turbulent flows that remain at sufficiently high Reynolds number, the influence of these molecular transport properties is confined to the smallest scales of motion and thus plays no direct role in setting the entrainment and mixing rates. With regard to kinematics, there is a volume source field produced by the Lagrangian rate of change in density due to heat release. Typically, however, the resulting induced velocity field is small in comparison with that induced by the underlying vorticity field. As for dynamical effects, heat release generates baroclinic vorticity from interactions of density gradients with both hydrostatic and hydrodynamic pressure gradients. The former, classically termed "buoyancy effects", can be quite pronounced even in flows without heat release, but are fundamentally different from the heat release effects considered here, which will be present even in the absence of any buoyancy. The latter, which depends on the magnitude of velocity gradients, typically becomes significant only in very high speed flows, whereas the heat release effects considered here will be present under all flow conditions.

Here we examine the influence of density changes due to heat release on the scaling laws that govern the flow itself. Turbulent shear flows typically grow only relatively slowly with downstream distance $x$, and for this reason such flows are classically treated as quasi-one-dimensional. Accordingly, local properties of the flow, such as entrainment and mixing rates, are determined by the outer variables $\delta(x)$ and $u(x)$, namely the length and velocity scales that characterize the local mean shear at any downstream location in the flow, as indicated in Figure 16. Consistent with this, the local range of spatial and temporal scales in the flow is characterized by a single local outer-scale Reynolds number $Re_\delta(x) \equiv u\delta/\nu$. Scaling laws for $\delta$ and $u$ can often be determined by simple dimensional reasoning and generally depend on the fluid densities even in flows without heat release. When heat release is present, the resulting density changes can therefore be expected to affect the flow through these scaling laws. This will be seen to be the dominant effect of heat release on entrainment and mixing rates, as well as other properties of the flow that are determined by the outer variables, in most high Reynolds number turbulent shear flows when buoyancy is negligible.

There are, in addition, other effects of heat release that go beyond the classical quasi-one-dimensional treatment of turbulent shear flows and which will not be addressed here. These include, for example, departures from strict self-similarity that arise as a result of lateral variations in the fluid properties due to heat release. Similarly, the increase in viscosity due to heat release can reduce $Re_\delta(x)$ sufficiently to render a flow transitional or even laminar, and such situations also will not be addressed here. Rather, we will confine attention to flows which remain fully turbulent and develop a general means to understand heat release effects within the classical quasi-one-dimensional treatment of turbulent shear flows. This, in turn, allows prediction of the resulting effects of heat release on entrainment and mixing rates, flame lengths, and other flow properties determined by the outer variable scalings.

## 5.2. General equivalence principle

### 5.2.1 *Temperature fields in flows without heat release*

Consider first the density field $\rho(\mathbf{x},t)$ created by differences in fluid temperatures in a flow without heat release. For any such adiabatic flow involving two fluids, denoted "0" and "1", respectively, at temperatures $T_0$ and $T_1$, enthalpy conservation allows the temperature field $T(\mathbf{x},t)$ that results from mixing of the two fluids to be everywhere related to the local mole fraction $X(\mathbf{x},t)$ of fluid "1". If the fluids can be taken as calorically perfect, then

$$T(\mathbf{x},t) = T_0 + \left(T_1 - T_0\right)\left(X(\mathbf{x},t) + \Pi\right) \quad , \tag{1}$$

with the nonlinearity in $X$ being

$$\Pi \equiv X(1-X)\left[\frac{\Delta C_p}{C_{p,0}}\right]\left\{\frac{1}{1+X\left[\dfrac{\Delta C_p}{C_{p,0}}\right]}\right\} \quad , \tag{2}$$

as shown schematically in Figure 17. The nonlinearity depends on the molar specific heat difference $\Delta C_p \equiv C_{p,1} - C_{p,0}$. The key point is that, when the $C_p$ difference in Eq. (2) is sufficiently small, $T(X)$ will be essentially linear whenever there is simple mixing without heat release between two fluids. If $\Delta C_p$ is not small, then Eq. (1) can be equivalently written in the $C_p$-weighted mole fraction, for which $T$ will be manifestly linear.

### 5.2.2 *Temperature fields in exothermic reacting flows*

Consider now the case when exothermic chemical reactions occur between the two fluids. Attention will be restricted to adiabatic flows, and activation energies that are sufficiently large for the reactions to be confined to a narrow range of mole fractions around the stoichiometric value $X_s$, where the temperature reaches its peak value $T_s$. This limits the application to reacting flows for which chemical nonequilibrium effects are sufficiently small that the resulting temperature is determined primarily by the extent of mixing as measured by $X$, which applies in most practical combustion situations.

The temperature field $T(\mathbf{x},t)$ can then again be related to the mole fraction field $X(\mathbf{x},t)$. As shown schematically in Figure 18, in this case it is convenient to equivalently view $T(X<X_s)$ as resulting from simple mixing, without reaction, of fluid "0" at temperature $T_0$ with stoichiometric products at $X = X_s$ and temperature $T_s$. Similarly $T(X>X_s)$ can be viewed as resulting from simple mixing between stoichiometric products at temperature $T_s$ and fluid "1" at temperature $T_1$. From the linearity noted above in the temperature field that results from simple mixing, $T(X)$ in such a reacting flow is thus necessarily piecewise linear, as indicated in Figure 18.

The bilinearity in $T(X)$ is demonstrated in Figures 19$a,b$ for hydrogen-air kinetics, for which the resulting high temperatures provide a test of the calorically perfect gas approximation, and the large differences in specific heats test the significance of the nonlinearity in Eq. (2). Even in these cases, $T(X)$ on either side of $X_s$ can be seen to be nearly linear. This piecewise linearity provides the basis for an equivalence between flows with and without reaction heat release.

### 5.2.3 *Effective temperatures and densities*

As shown in Figure 20, from the piecewise linearity of $T(X)$ in such exothermic reacting flows, wherever $X(\mathbf{x},t) > X_s$ the temperature $T(\mathbf{x},t)$ will be equivalent to that which would result

from simple mixing without reaction between an inert fluid "1" at its actual temperature $T_1$ and density $\rho_1$, and an inert fluid "0" at an effective elevated temperature $(T_0)_{eff}$ given by

$$(T_0)_{eff} \equiv T_1 + \frac{T_s - T_1}{1 - X_s} \quad , \tag{3a}$$

and hence at a corresponding effective density

$$(\rho_0)_{eff} = \rho_0 \left( \frac{T_0}{(T_0)_{eff}} \right) \quad . \tag{3b}$$

Both the reacting flow and the fictitious nonreacting flow will have the same temperature fields $T(\mathbf{x},t)$ and hence density fields $\rho(\mathbf{x},t)$ wherever $X(\mathbf{x},t) > X_s$.

Similarly, wherever $X(\mathbf{x},t) < X_s$ the temperature $T(\mathbf{x},t)$ in the reacting flow will be equivalent to that produced by mixing without reaction between an inert fluid "0" at its actual temperature $T_0$ and density $\rho_0$, and an inert fluid "1" at $(T_1)_{eff}$ given by

$$(T_1)_{eff} \equiv T_0 + \frac{T_s - T_0}{X_s} \quad , \tag{4a}$$

with corresponding effective density

$$(\rho_1)_{eff} = \rho_1 \left( \frac{T_1}{(T_1)_{eff}} \right) \quad . \tag{4b}$$

Thus the density field $\rho(\mathbf{x},t)$ in a reacting flow at values of $X(\mathbf{x},t)$ above (or below) $X_s$ will be the same as that in a fictitious nonreacting flow with the appropriate fluid density replaced by its effective value in Eq. (3b) (or Eq. (4b)) and with the other fluid density kept at its true value.

### 5.2.4 *Equivalence between reacting and nonreacting flows*

Under these conditions, the effects of density changes due to heat release on the outer variables in an exothermic reacting flow should be deducible from the scaling laws that apply in the corresponding nonreacting flow by replacing the appropriate fluid density with its effective value in Eqs. (3b) or (4b). Thus, based on the equivalence noted in Figure 20, at values of the downstream distance $x$ for which $X(\mathbf{x},t)$ is predominantly above $X_s$, the scaling laws for the exothermic flow are obtained from those for the corresponding nonreacting flow by replacing $\rho_0$ with $(\rho_0)_{eff}$ from Eq. (3b). Similarly, at $x$ values for which $X(\mathbf{x},t)$ is predominantly below $X_s$, the effects of density variations due to heat release would be accounted for by replacing $\rho_1$ with $(\rho_1)_{eff}$ from Eq. (4b) in the scaling laws for the local outer variables $\delta(x)$ and $u(x)$ in the corresponding nonreacting flow.

The effective densities in Eqs. (3b) and (4b) require only the effective temperatures in Eqs.

(3a) and (4a). These, in turn, depend on the stoichiometric temperature $T_s$ and mole fraction $X_s$. It will be seen below that this equivalence principle between reacting and nonreacting flows accurately predicts the effects of heat release on the outer variables of turbulent shear flows under conditions for which buoyancy effects are negligible.

## 5.3. Heat release effects in axisymmetric turbulent jets

In this section the general equivalence principle from §5.2 is applied to determine the effects of combustion heat release on axisymmetric turbulent jets. The resulting predicted heat release effects are then compared with experimental data from nonbuoyant turbulent jet diffusion flames to assess the validity of the equivalence conjectured above between reacting and nonreacting turbulent shear flows.

### 5.3.1 Scaling laws for nonreacting jets

In the self-similar far field of nonreacting axisymmetric turbulent jets, the outer variables $\delta(x)$ and $u(x)$ are the mean flow width and centerline velocity, as indicated in Figure 16. Scaling laws for these can be found by dimensional reasoning in terms of the jet source momentum flux $J_0$, which is an invariant of the flow, the ambient fluid density $\rho_\infty$, and the downstream distance $x$ as

$$\delta = 0.44\, x \tag{6a}$$

$$u = 7.3\left(J_0/\rho_\infty\right)^{1/2} x^{-1} \tag{6b}$$

with the scaling constants obtained from experimental data (e.g., Wygnanski & Fiedler 1969). Here $\delta$ is the full width where the mean velocity is 5% of its local centerline value, with the scaling constant for other definitions obtained from the mean profile.

It is popular to equivalently write Eq. (6b) in terms of an "exit velocity" $u_0 \equiv (J_0/m_0)$, where $m_0$ is the jet source mass flux, as

$$u/u_0 = 6.5\left(x/d^*\right)^{-1} \tag{7}$$

where $d^*$ is the far field equivalent source diameter, given by

$$d^* \equiv \frac{2\, m_0}{\left(\pi \rho_\infty J_0\right)^{1/2}} \quad . \tag{8}$$

For jets issuing with uniform density and velocity distributions from circular nozzles, as is sometimes the case, $d^*$ reduces to

$$d^* = \left(\frac{\rho_0}{\rho_\infty}\right)^{1/2} d_0 \ , \tag{9}$$

where $d_0$ is the physical source diameter and $\rho_0$ is the jet fluid density. Thring & Newby (1953) first proposed $d^*$, called the "momentum diameter", to account for density differences between the

jet and ambient fluids in axisymmetric turbulent jets without heat release.

Ricou & Spalding (1961) investigated the effects of jet and ambient fluid densities on the entrainment rate $E(x) \equiv dm(x)/dx$, where $m(x) \sim \rho_\infty u(x)\, \delta^2(x)$ is the mass flux, of isothermal turbulent jets. Their experimental results confirmed the Thring and Newby proposal that the equivalent diameter $d*$ in Eqs. (8) and (9) provided the proper accounting for density effects, eliminating apparent differences in the scaling laws for nonreacting jets with matched and unmatched densities. In effect Ricou and Spalding demonstrated that, in the absence of heat release, the scaling of jets with matched or unmatched densities could be unified in a single scaling law via $d*$.

### 5.3.2  Observed effects of combustion heat release

Burning jets of propane and hydrogen were briefly examined in the same investigation by Ricou & Spalding (1961). Their results showed a reduction of up to 30% in the mass entrainment rate $E(x)$ of burning jets relative to the corresponding isothermal jets. Similar differences between isothermal and burning jets can also be seen in the mean centerline velocity decay in Figure 21 from measurements of Chigier & Strokin (1974), Takagi et al (1981), and Muñiz & Mungal (1995) under conditions for which buoyancy effects are essentially negligible. In each case, the velocity in the burning jet decreases more slowly with $x$ than in the nonburning jet under otherwise identical conditions. The lower rates of velocity decay in these data from turbulent jet flames are consistent with the reduced entrainment rate due to heat release noted by Ricou and Spalding. Such effects of heat release on velocity and conserved scalar decay rates in jet flames have been noted since the earliest studies of Hawthorne, Weddel & Hottel (1949), Thring & Newby (1953), Sunavala, Hulsa & Thring (1957) and Kremer (1967). Many studies have also noted the attendant increase in jet flame length over that which would be expected from the entrainment and mixing rate in nonburning jets.

Observations such as these have led some studies to conclude that fundamental differences exist between burning and nonburning jets as a consequence of heat release effects. In §5.3.3 and §5.3.4 we will assess if the scaling laws for both can be reconciled when account is taken, in the manner described in §5.2.4, of the density changes due to combustion heat release.

### 3.3  Application of the general equivalence principle

We will choose $X$ so that pure jet fluid corresponds to $X = 1$ as in Figure 16. Then for values of $x$ sufficiently far upstream of the flame tip, most of the fluid in the jet is at $X > X_s$. In accordance with the equivalence principle developed in §5.2, we would extend the scaling laws for nonreacting turbulent jets from §5.3.1 to account for the effects of heat release by replacing $\rho_\infty$ in

Eq. (6) through Eq. (9) with $(\rho_\infty)_{eff}$ in Eq. (3b). The scaling laws for both burning and nonburning axisymmetric turbulent jets should then be identical in the resulting "extended momentum diameter" $d^+$ as

$$\delta = 0.44\, x \tag{10a}$$

$$u/u_0 = 6.5\left(x/d^+\right)^{-1} \quad , \tag{10b}$$

where from Eq. (9)

$$d^+ \equiv \left(\frac{\rho_0}{(\rho_\infty)_{eff}}\right)^{1/2} d_0 \tag{11a}$$

or, in its more general form from Eq. (8),

$$d^+ \equiv \frac{2\,m_0}{\left(\pi(\rho_\infty)_{eff}\, J_0\right)^{1/2}} \quad . \tag{11b}$$

Note that $d^+ \equiv d^*$ for nonburning jets. In this manner, the general equivalence principle of §5.2, when applied to axisymmetric turbulent jets, extends the classical scaling laws for nonburning jets to burning jets, and thereby unifies their scaling laws via $d^+$ in an analogous way as did the classical momentum diameter $d^*$ of Thring & Newby (1953) and Ricou & Spalding (1961) for nonburning jets with matched and unmatched densities.

Similarly, for values of $x$ sufficiently far downstream of the flame tip, the fluid moving with the jet is at mole fractions $X < X_s$. In accordance with the equivalence principle in §5.2, the scaling laws applicable to such large values of $x$ would be obtained by instead replacing $\rho_0$ in Eq. (6) through Eq. (9) with $(\rho_0)_{eff}$ in Eq. (4b). Thus Eqs. (10a,b) would still apply, but the extended momentum diameter $d^+$ in that case becomes

$$d^+ \equiv \left(\frac{(\rho_0)_{eff}}{\rho_\infty}\right)^{1/2} d_0 \quad . \tag{12}$$

### 5.3.4 *Comparisons with experimental results*

The results in §5.3.3 suggest that the scaling laws for both nonburning and burning axisymmetric turbulent jets will be identical in terms of the extended momentum diameter $d^+$ in Eq. (11). Thus, for instance, the mean centerline velocity scaling for burning, as well as nonburning, jets would be given by Eq. (10b). For burning jets this yields a reduction in the velocity decay rate that depends on $(\rho_\infty)_{eff}/\rho_\infty$, and hence on $(T_\infty)_{eff}$.

To assess the validity of the equivalence principle and the extended jet scaling laws that it implies, the result in Eq. (10b) is shown, for both burning and nonburning jets, by the lines in

Figure 22. The symbols give the data for burning and nonburning jets from Figure 21. Values of $X_s$ and $T_s$, determined by the jet and ambient fluid compositions, are given for each case in Table 1 together with the momentum diameter $d*$ for nonburning jets and $d^+$ for burning jets. Figure 22 shows that the agreement for burning jets (solid line versus open symbols) is about as good as the classical scaling of Thring and Newby (1953) and Ricou & Spalding (1961) is for nonburning jets (dashed line versus solid symbols).

In Figure 22 and Table 1 it is especially noteworthy to compare the effects of fuel dilution by Muñiz & Mungal (1995) with the pure fuel used by Chigier & Strokin (1974). The table shows that the dilution leads to significant differences in $X_s$ and $T_s$, but the two effects offset each other (see Figure 20) to give roughly the same $(T_\infty)_{eff}$. Indeed Figures 22a and 22c suggest similar heat release effects in both cases, despite the dilution, with the differences between these cases being solely due to the different values of $\rho_0$. Furthermore, Table 1 shows that dilution of the fuel by Takagi et al (1981) produces even larger changes in $X_s$ and $T_s$, leading to a much higher $(T_\infty)_{eff}$, yet the agreement in Figure 22b is equally good as in the other two cases.

Figure 22 and Table 1 also show that ad hoc use of $T_s$ in place of $(T_\infty)_{eff}$, as has been proposed in certain heuristic attempts to account for exothermicity in jets, would lead to comparatively inaccurate prediction of heat release effects. The difference is clearest in the case of Takagi et al (1981), where these temperatures differ by almost a factor of two (e.g., see Figure 19b). The results in Figure 22 suggest that the $d^+$ scaling in §5.3.3, based on the general equivalence principle in §5.2, appears to accurately predict the effect of heat release on the velocity decay in turbulent jets.

A further comparison is possible from the data of Flury & Schlatter (1995), who measured the centerline velocity decay in axisymmetric turbulent jet flames of hydrogen, diluted with various levels of helium, burning in air under conditions for which effects of buoyancy and coflow are negligible. Their results are compared with Eq. (10b) in Figure 23, with relevant parameters in Table 1. The classical isothermal scaling is shown by the dashed lines, and the solid lines give the extended scaling for jets with heat release. For the burning jets, dilution changes both $X_s$ and $T_s$. These again act to partly offset each other, but in this case produce an increase in $(T_\infty)_{eff}$ with increasing helium dilution. In each case, the net effect on the velocity decay in the burning jet appears in good agreement with the extended scaling in Eq. (10b). Here, too, the differences between $T_s$ and $(T_\infty)_{eff}$ are quite large. Note also that $T_s$, unlike $(T_\infty)_{eff}$, decreases with increasing dilution, and thus ad hoc methods based on substituting $T_s$ for $T_\infty$ would produce the opposite effect on the rate of velocity decay with increasing dilution from that obtained by the present equivalence principle.

All of these data for centerline velocity decay in both burning and nonburning jets are shown in terms of $(x/d^+)$, as indicated by Eq. (10$b$), in Figure 24. The agreement with the extended scaling in the far field, shown by the solid line, is seen to be equally good for the burning and nonburning jets, indicating that the general equivalence principle in §5.2 appears to correctly extend the scaling laws for nonburning jets to predict the effects of heat release in turbulent jet flames.

Moreover, since the scaling for $\delta(x)$ in Eq. (10$a$) does not depend on either the jet or ambient fluid densities, the equivalence principle indicates that, in the absence of significant buoyancy, there will be no effect of heat release on the flow width. To test this, Figure 25 shows data for $\delta(x)$ from a wide range of burning and nonburning axisymmetric turbulent jets, together with the far field scaling indicated by Eq. (10$a$). Note that the agreement of this scaling with data from burning jets is again about as good as is that between nonburning jets and the classical scaling, in agreement with the equivalence principle in §5.2.

Furthermore, the mass flux scaling $m(x)$ is obtained directly from the centerline velocity and flow width scalings, as noted in §5.3.1. As a consequence, the centerline conserved scalar decay follows as $\zeta(x) \sim m_\zeta / m(x)$, where $m_\zeta$ is the mass flux of scalar from the jet source. For nonburning jets it is popular to write this in terms of an "exit scalar value" $\zeta_0 \equiv (m_\zeta/m_0)$ as

$$\zeta/\zeta_0 = 5.4 \left(x/d^*\right)^{-1} \quad . \tag{13}$$

From the equivalence principle, this scaling would be extended to burning and nonburning jets by replacing $\rho_\infty$ with $(\rho_\infty)_{eff}$, giving

$$\zeta/\zeta_0 = 5.4 \left(x/d^+\right)^{-1} \quad . \tag{14}$$

To test this, Figure 26 compares the centerline conserved scalar decay $\zeta(x)$ measured in nonbuoyant turbulent jet flames and in turbulent jets without heat release. The solid line gives the unified scaling in Eq. (14), and the agreement of data from both burning and nonburning jets with this scaling further supports the general equivalence principle in §5.2.

Finally, from the conserved scalar scaling above, the flame length $L$ in burning jets is determined by the downstream distance $x$ at which the maximum scalar value, which scales with $\zeta(x)$, reaches the stoichiometric value $\zeta_s$. Thus from Eq. (14)

$$L/d^+ = 10 \left(\varphi + 1\right) \quad , \tag{15}$$

where $\varphi$ is the mass ratio of ambient-to-jet fluids in a stoichiometric mixture, and the constant is from measurements of Dahm & Dimotakis (1987) in nonburning jets (see their Figure 1). From Eq. (15), the flame lengths of burning jets would thus be longer than those indicated by mixing in

34

isothermal jets by the factor $d^+/d^* = [(T_\infty)_{eff} / T_\infty]^{1/2}$. As Table 1 reveals, this ratio is typically about three for most hydrocarbon fuels and for a wide range of dilutions. The result in Eq. (15) is in good agreement with available flame length data from nonbuoyant turbulent jet diffusion flames; e.g., see Figures 1 and 2 of Blake & McDonald (1993), who used *ad hoc* replacement of $T_\infty$ by $T_s$, instead of $(T_\infty)_{eff}$ suggested by the equivalence in §5.2.

## 5.4. Heat release effects in planar turbulent jets

The equivalence in §5.2 determines the effects of heat release on the outer variable scaling laws for any turbulent shear flow; in this section we will apply it to planar turbulent jets. Rehm & Clemens (1996, 1998) have experimentally documented effects of heat release due to burning in a planar turbulent jet issuing from a slot of width $h$ and effectively infinite span under conditions for which buoyancy effects are negligible. Their data provide a further opportunity to assess the validity of the general principle proposed here for equivalence in the scaling laws of nonburning and burning flows and to assess the accuracy of the heat release effects predicted by this principle.

### 5.4.1 Scaling laws for nonreacting planar jets

The outer variables $\delta(x)$ and $u(x)$ in the self-similar far field of nonreacting planar turbulent jets scale with the jet source momentum flux per unit span $J_0$ and the ambient fluid density $\rho_\infty$ as

$$\delta \sim x \tag{16a}$$

$$u \sim \left(J_0/\rho_\infty\right)^{1/2} x^{-1/2} \quad ; \tag{16b}$$

(e.g., Gutmark & Wygnanski 1976). As in §5.3.1, it is common to equivalently write this scaling in terms of a far field equivalent slot width $h^*$ as

$$u/u_0 \sim \left(x/h^*\right)^{-1/2} \tag{17}$$

where

$$h^* \equiv \frac{m_0^2}{\left(\rho_\infty J_0\right)} \quad . \tag{18}$$

For jets issuing with uniform density and velocity, Eq. (18) reduces to

$$h^* = \left(\frac{\rho_0}{\rho_\infty}\right) h_0 \tag{19}$$

where $h_0$ is the physical slot width and $\rho_0$ is the jet fluid density.

These outer variables set the scaling for the mass flux per unit span as $m(x) \sim \rho_\infty u(x) \delta(x)$, with the scaling for the centerline conserved scalar then following as $\zeta(x) \sim m_\zeta/m(x)$ as noted in §5.3.4. For nonreacting planar turbulent jets this scaling gives

35

$$\zeta/\zeta_0 = 5.4 \left(x/h*\right)^{-1/2} \quad , \tag{20}$$

where the scaling constant comes from experimental data.

### 5.4.2  *Application of the general equivalence principle*

Defining $X$ so that pure jet fluid corresponds to $X = 1$ as in Figure 16, then at values of $x$ sufficiently upstream of the flame tip most of the fluid in the jet is at $X > X_s$. Accordingly the equivalence principle in §5.2 indicates that the scaling laws in §5.4.1 for the nonreacting jet can be extended to burning jets by replacing $\rho_\infty$ in Eq. (16) through Eq. (20) with $(\rho_\infty)_{eff}$ in Eq. (3$b$). Thus, for example, the scaling for the centerline conserved scalar in Eq. (20) becomes

$$\zeta/\zeta_0 = 5.4 \left(x/h^+\right)^{-1/2} \quad , \tag{21}$$

with $h^+$, from Eq. (19), becoming

$$h^+ = \left(\frac{\rho_0}{\left(\rho_\infty\right)_{eff}}\right) h_0 \quad . \tag{22}$$

For nonburning burning jets $h^+ = h*$; thus the scaling laws for both nonburning and burning jets should be identical in terms of $h^+$. Following the same reasoning as in §5.3.4, the flame length $L$ in this case scales as

$$L/h^+ \sim \left(\varphi + 1\right)^2 \quad . \tag{23}$$

Note that, owing to the different exponents in Eq. (11$a$) and Eq. (22), the effect of heat release on flame length is far more pronounced in planar jets than in axisymmetric jets.

### 5.4.3  *Comparisons with experimental results*

Figure 27 shows the data of Rehm & Clemens (1996, 1998) for the centerline conserved scalar decay in burning and nonburning planar turbulent jets in terms of the classical equivalent slot width $h*$ in Eqs. (18) and (19). Note that results for the two nonburning jets, which have different values of $\rho_0$, show good agreement in the classical $h*$ scaling in Eq. (20). In contrast, results from the burning jet show a much lower rate of mixing and do not appear consistent with the $h*$ scaling that governs the nonreacting flow.

When these same data are plotted as in Eq. (21), in terms of $h^+$, then the results for the burning and nonburning jets are seen in Figure 28 to follow the same scaling, in agreement with the equivalence principle in §5.2. The solid line gives the far field scaling in Eq. (21). Note that the agreement of the present $h^+$ scaling with data from the burning jet is comparable to that of the classical $h*$ scaling with the data from the nonburning jets. When presented in this form, the data from the burning jet can be seen to just barely reach the far field. Even in the transition region, the data from the burning and nonburning jets, when scaled by $h^+$, appear to be in agreement.

We conclude that the equivalence principle in §5.2 accurately predicts the effects of combustion heat release on the outer variable scalings in planar turbulent jets, as it did for axisymmetric turbulent jets in §5.3, under conditions for which buoyancy effects are negligible.

### 5.5. Heat release effects on jet near field length

The scaling laws for turbulent jets in §5.3 and §5.4 apply in the far field, at values of $x$ sufficiently large that the only remaining dynamically relevant aspect of the jet source is its momentum flux, which remains invariant when buoyancy effects are negligible. By contrast, the near field, or potential core region, refers to values of $x$ sufficiently small that the centerline velocity $u(x)$ and conserved scalar $\zeta(x)$ remain essentially constant at their source values $u_0$ and $\zeta_0$. The transition from this near field scaling to the far field scaling in Eqs. (14) and (21) can be seen, for example, in Figures 24, 26 and 28. The length $l$ of the near field can thus be associated with the point at which the two scalings cross and is known to be affected by heat release. For example, Savas & Gollahalli (1986) and Clemens & Paul (1995) have shown dramatic differences in the potential core region of burning and nonburning axisymmetric turbulent jets under otherwise identical conditions. Their results indicate, among other effects, a large increase in the length of the near field under burning conditions and striking changes in the vortical structure of the potential core region (e.g., see Figures $1a,b$ of Savas & Gollahalli 1986).

These changes in the near field due to heat release are likely to be a result of many different factors, some of which were noted in §5.1 and are discussed in detail by Savas and Gollahalli and by Clemens and Paul; however, owing to the universality of the jet scalings in Eqs. (14) or (21), the transition between the near and far field scalings must occur at the fixed value $(l/d^+) = 5.4$, or $(l/h^+) = 5.4$, irrespective of the level of heat release. For axisymmetric turbulent jets, in terms of the observable momentum diameter the resulting near field length becomes

$$(l/d^*) = 5.4 \left( \frac{(T_\infty)_{eff}}{T_\infty} \right)^{1/2} , \qquad (24)$$

while for planar turbulent jets this becomes

$$(l/h^*) = 5.4 \left( \frac{(T_\infty)_{eff}}{T_\infty} \right) . \qquad (25)$$

Note that Eqs. (24) and (25) indicate an increase in the length of the near field due to heat release, with the effect being more pronounced for planar jet flames.

For axisymmetric turbulent jets of typical hydrocarbon fuels issuing into air, values of $(T_\infty)_{eff}$

such as in Table 1 indicate that the near field will typically be about 3 times longer in burning jets than in nonburning jets. This result, from Eq. (24), agrees with the available qualitative observations in axisymmetric jets of Yule *et al* (1981), Savas & Gollahalli (1986), and Clemens & Paul (1995), and is further supported by the quantitative agreement evident in the transition region in Figure 24 between data from burning jets (open symbols) and nonburning jets (solid symbols). Similarly, from Eq. (25) and Table 1, in planar turbulent jets the predicted effect of heat release on the near field length is an increase by typically about a factor of 10, which is also in good quantitative agreement in Figures 27 and 28 with the data of Rehm & Clemens (1996, 1998) from burning and nonburning jets.

The increased near field lengths due to heat release in Eqs. (24) and (25) require an attendant reduction in the growth rate of the mixing layer on the jet periphery in the near field. This reduced growth rate, in turn, implies changes in the vortex size and spacing within the mixing layer that are also qualitatively consistent with the effects due to heat release in Figures 1a and 1b of Savas & Gollahalli (1986) and in Figures 5 and 7 of Clemens & Paul (1995).

The simple equivalence principle in §5.2 appears to correctly predict the dominant observed effects of heat release on the length and vortex structure of the near fields of planar and axisymmetric turbulent jet flames; however, there are likely to be other effects of heat release that may play an additional role in setting details of the vortex size and structure in the near field of jets (e.g., Yamashita, Kushida & Takeno 1990; Takeno 1994).

## 5.6. Concluding remarks

The equivalence introduced here, based on the principle in Figure 20, accounts for the effects of heat release on turbulent shear flows through the scaling laws for the local outer variables that govern the corresponding nonreacting flow. Its application is restricted to conditions under which buoyancy effects are negligible. Under such conditions, the results in §5.3 through §5.5 indicate that the heat release mechanism considered here is the principal effect of exothermicity on the outer variable scalings in most turbulent reacting flows. It was seen here to accurately predict the dominant heat release effects, in both the near and far fields, of planar and axisymmetric turbulent jet flames over a range of fuels and dilutions.

This general principle, developed in §5.2 (see also Tacina & Dahm 1996), is based on the piecewise linear form of $T(X)$ in the mole fraction $X$, which is demanded by enthalpy conservation in a reacting flow under the conditions noted in §5.2.1 and §5.2.2. As noted in §5.2.1, a linear $T(X)$ is indicative of simple fluid mixing, without reaction. Thus, on either side of the stoichiometric mole fraction $X_s$, the temperature field $T(X)$ in the reacting flow is equivalent to that

which would occur in a corresponding nonreacting flow with the temperature of one of the fluids raised to a fictitious elevated value given in Eqs. (3a) or (4a). This is done in practice by replacing one of the two fluid densities in the outer variable scaling laws for the corresponding nonreacting flow with the effective value given in Eqs. (3b) or (4b) that corresponds to this elevated temperature. The density field $\rho(\mathbf{x},t)$ in the fictitious nonreacting flow will then be identical to that which occurs in the exothermic reacting flow wherever the mole fraction field $X(\mathbf{x},t)$ is above (or below) the stoichiometric value $X_s$. In this manner, the dominant effects of density changes due to heat release in the exothermic flow are incorporated in the nonreacting flow.

Application of this principle was demonstrated for axisymmetric turbulent jets in §5.3. In that case it led to a generalized momentum diameter $d^+$ that extends the classical Thring & Newby (1953) and Ricou & Spalding (1961) momentum diameter $d^*$ to exothermic flows. In terms of $(x/d^+)$, the scaling laws for the outer variables $u$ and $\delta$ in jets with and without heat release become identical. For values of $x$ sufficiently smaller than the flame length, $d^+$ is obtained from $d^*$ by replacing $\rho_\infty$ with $(\rho_\infty)_{eff}$, while for $x$ values sufficiently beyond the flame tip, it is instead $\rho_0$ that is replaced by $(\rho_0)_{eff}$. Doing so was seen in Figures 22 through 26 to accurately predict the reduction in entrainment and mixing rates observed due to heat release in turbulent jet flames for a variety of fuels and dilutions. These, in turn, determine the effect of heat release on the flame length as noted in Eq. (15). Similarly, when this equivalence principle was applied to planar turbulent jets in §5.4, it led to an extended momentum width $h^+$ that from Figures 27 and 28 was seen to correctly predict the much stronger effect of heat release on the entrainment and mixing rate in that flow as well, with the effect on planar turbulent jet flame lengths given in Eq. (23).

Application of the equivalence principle also led to the observation that the near field length $(l/d^+)$, or $(l/h^+)$, must scale with the point at which the near and far field scalings cross, as in Figures 24, 26 and 28. This led to the results in Eqs. (24) and (25) for the effect of heat release on the near field length, which indicate a much larger increase due to heat release in planar turbulent jets than is the case for axisymmetric jets. The results were found to be in good agreement with available observations and measurements in the transition region of both planar and axisymmetric turbulent jet flames.

This equivalence principle will, of course, fail if used outside the range over which its physical assumptions apply. Most obvious among these is when buoyancy effects due to heat release are no longer negligible, and under such conditions the method is not meant to be applied. Similarly, when the increase in viscosity due to heat release produces a sufficient reduction in Reynolds number for the flow to become transitional or laminar (e.g., Takeno 1994), then the equivalence no longer applies. Near the flame tip, where mole fractions are centered around the

stoichiometric value $X_s$, the local mole fraction field $X(\mathbf{x},t)$ is not dominated by either of the linear branches of $T(X)$. The underlying equivalence then fails, and the method is again not meant to be applied. Furthermore, in situations for which the underlying adiabatic assumption is sufficiently violated that the temperature is no longer adequately determined by the mole fraction, as could potentially occur in very strongly radiating flows or in flows with large heat extraction, then the underlying assumptions fail, and the method is not meant to be applied. A similar limitation could apply if differential diffusion effects are sufficiently pronounced that the temperature is no longer adequately determined by the mole fraction. Moreover, if the reactions are not sufficiently fast to avoid chemical nonequilibrium effects, such as might occur in very high speed flows where local extinction effects can be significant, then the temperature field will no longer be simply determined by the mole fraction, and the method should not be applied. Finally, if temperatures in the reacting flow are high enough for dissociation effects to become significant, such as can occur in oxygen-enriched combustion, for example, then $T(X)$ will no longer be piecewise linear, and the method is not meant to be applied. However, in most practical combustion applications, the equivalence principle will be applicable and appears to capture the dominant effects of heat release on the outer variables and thus the resulting entrainment and mixing properties, of turbulent shear flows.

The notion of extending the scaling laws for nonreacting flows to account for heat release effects by a change in ambient fluid density is not entirely new, although previous attempts to do this have lacked the rigorous basis developed here. Hawthorne *et al* (1949) noted the lower entrainment rate in burning jets in the absence of buoyancy and thus used $T_s$ in place of $T_\infty$ in their expression for flame lengths in an attempt to account for this. After noting the errors that result when applying the isothermal density correction of Thring & Newby (1953) to turbulent jet flames, several studies have similarly advocated heuristically treating a jet flame as a cold, high-density jet entraining hot, low-density ambient gases at the flame temperature $T_s$ (e.g., Rhine & Tucker 1991). That *ad hoc* approach bears some resemblance to the formal result obtained here by applying the general equivalence principle of §5.2 to turbulent jets but differs in the simplistic way in which it assigns the fictitious ambient fluid temperature. Moreover, it lacks the generality or rigorous basis that comes from the fundamental equivalence in Figure 20. Accordingly, when the stoichiometric mole fraction is not small, as in some of the cases in Table 1, the predictions obtained with such previous heuristic approaches can significantly underestimate the effects of heat release. Furthermore, as noted in §5.3.4, the *ad hoc* use of $T_s$ in place of $T_\infty$ in some circumstances even predicts the opposite effects of heat release from those predicted by the present equivalence principle, as in the case of increasing helium or nitrogen dilution of hydrogen fuel burning in air.

Finally, the equivalence principle developed here to account for heat release effects is also

somewhat similar in spirit to a set of methods initiated by van Driest to account for compressibility effects on the scaling of turbulent boundary layers (e.g., see Smits *et al* 1989). That approach is also based on accounting for property variations; in that case the effects of the temperature increase due to compressibility on viscosity $\mu$ and density $\rho$. This allows the scaling laws for incompressible boundary layers to be extended to compressible boundary layers, in a somewhat similar manner as the scaling laws for nonreacting turbulent shear flows are here extended to exothermic flows via the present rescaling of fluid density. The success of these two approaches suggests that it might be possible to develop such equivalence principles more broadly. It may even be possible to determine the effects of density changes in compressible turbulent shear flows via a simple rescaling of densities in the scaling laws for the corresponding incompressible flow. This would allow compressibility effects in turbulent shear flows to be determined in much the same way as the present equivalence principle determines heat release effects on turbulent shear flows.

| | Jet Fluid | $u_0$ (m/s) | $d_0$ or $h_0$ (mm) | $d^*$ or $h^*$ (mm) | $X_s$ (—) | $T_s$ (K) | $(T_\infty)_{eff}$ (K) | $d^+$ or $h^+$ (mm) |
|---|---|---|---|---|---|---|---|---|
| Barlow & Carter (1994) | $H_2$ | 288 | 3.75 | 0.98 | 0.296 | 2384 | 3259 | 3.25 |
| Cheng et al (1992) | $H_2$ | 680 | 2.0 | 0.53 | 0.296 | 2384 | 3259 | 1.73 |
| Chigier & Strokin (1974) | $CH_4$ | 20 | 5.0 | 3.71 | 0.096 | 2226 | 2430 | 10.57 |
| Flury & Schlatter (1995) | $H_2$ | 296 | 3.75 | 0.98 | 0.296 | 2384 | 3259 | 3.25 |
| Flury & Schlatter (1995) | $0.8\ H_2 + 0.2\ He$ | 346 | 3.75 | 0.98 | 0.346 | 2324 | 3396 | 3.31 |
| Flury & Schlatter (1995) | $0.6\ H_2 + 0.4\ He$ | 342 | 3.75 | 0.98 | 0.414 | 2228 | 3590 | 3.41 |
| Muñiz & Mungal (1995) | $0.4\ CH_4 + 0.6\ N_2$ | 20 | 4.5 | 4.33 | 0.209 | 2075 | 2543 | 12.31 |
| Rehm & Clemens (1996, 1998) | $0.5\ H_2 + 0.5\ N_2$ | 135 | 1.0 | 0.62 | 0.457 | 2025 | 3475 | 7.19 |
| Takagi et al (1981) | $0.4\ H_2 + 0.6\ N_2$ | 55 | 4.9 | 4.19 | 0.514 | 1872 | 3537 | 14.39 |

Table 1. Measurements used in §5.3 through §5.5 for comparison with heat release effects predicted by the equivalence principle in §5.2, showing jet fluid composition in mole fractions, jet exit conditions, momentum diameter $d^*$ (or width $h^*$), stoichiometric jet fluid mole fraction $X_s$, adiabatic flame temperature $T_s$, effective ambient fluid temperature $(T_\infty)_{eff}$ from Eq. (3a), and extended diameter $d^+$ (or width $h^+$) from Eqs. (11a) or (22). Ambient fluid in all cases is air at $T_\infty \approx 300$ K.
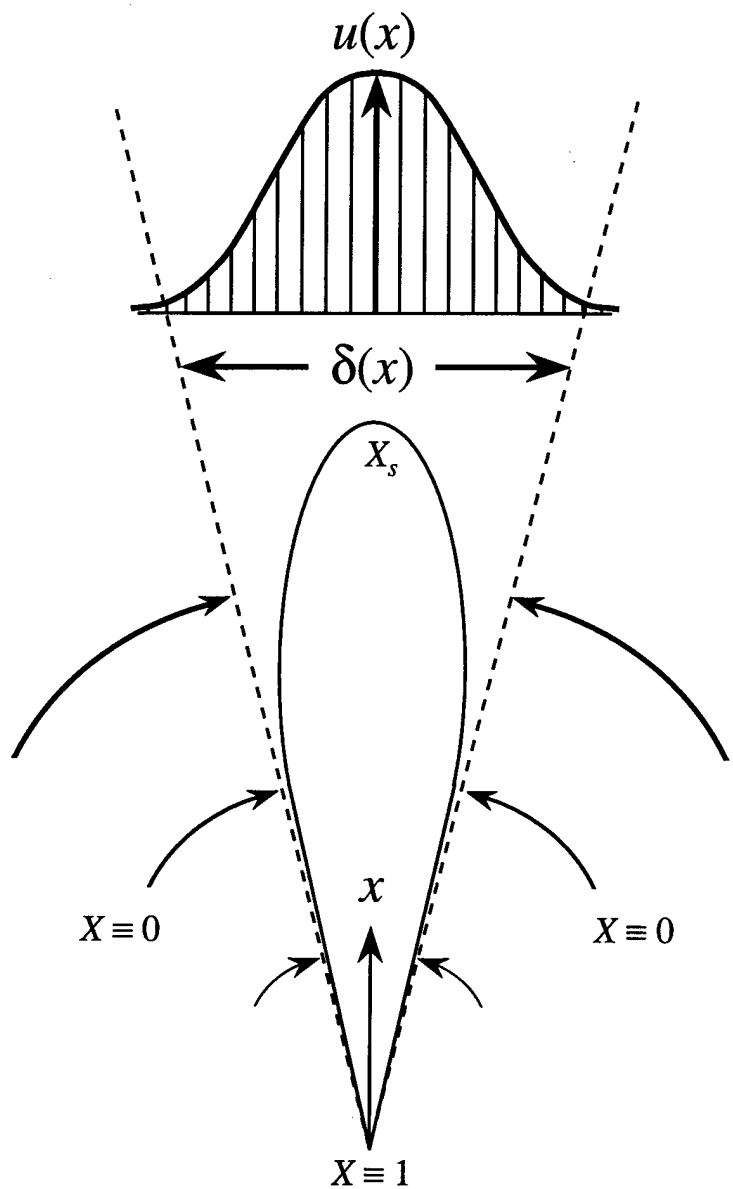
Figure 16. Schematic indicating local outer variables $\delta(x)$ and $u(x)$ that characterize the mean shear at any downstream location $x$ in a turbulent shear flow, in this case a turbulent jet. Within the stoichiometric contour, fluid is typically at mole fractions $X(\mathbf{x},t) > X_s$.

Figure 18. Variation of temperature $T(x,t)$ with mole fraction $X(x,t)$ in an exothermic reacting flow, showing stoichiometric temperature $T_s$ at mole fraction $X_s$. Note that the linear form of $T(X)$ on either side of $X_s$ is indicative of simple mixing, without reaction, of either fluid with stoichiometric products.



Figure 17. Variation of temperature $T(x,t)$ with mole fraction $X(x,t)$ in a nonreacting flow formed by two fluids at temperatures $T_0$ and $T_1$, corresponding respectively to mole fractions $X = 0$ and $X = 1$. The linear form of $T(X)$ is indicative of simple mixing without reaction.

44
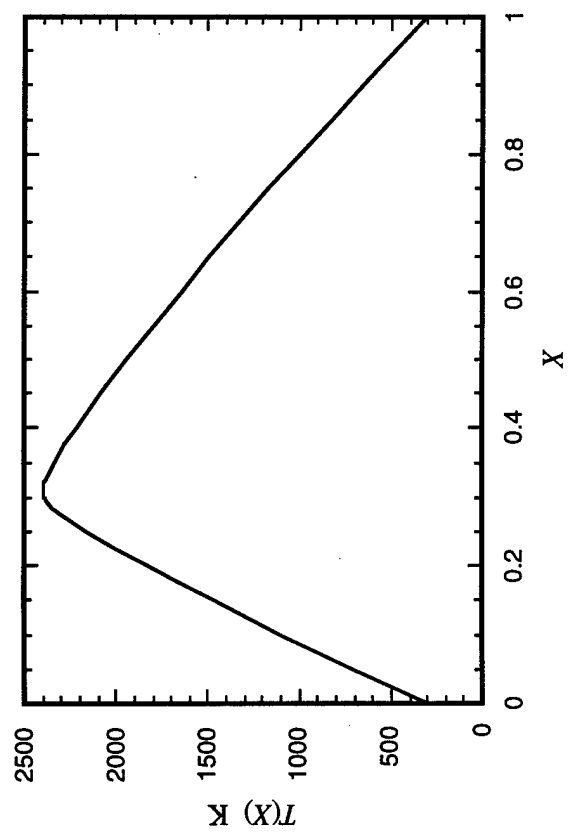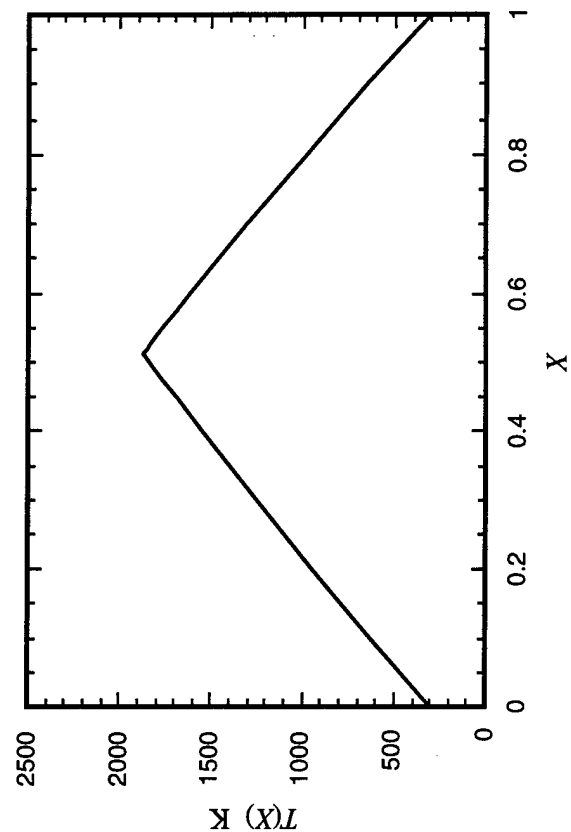
Figure 19a. Adiabatic equilibrium temperature $T$ due to mixing and chemical reaction of pure $H_2$ (fluid "1") and air (fluid "0"), both initially at 300 K, shown against the mole fraction $X$ of fluid "1". Results are from detailed chemistry, and correspond to several cases in Table 1. Note that, even for these relatively high temperatures and large differences in specific heats, $T(X)$ is nearly linear on either side of $X_s$.



Figure 19b. Similar to Figure 19a, but for mixing and reaction of 40% $H_2$ + 60% $N_2$ with air, corresponding to Takagi et al (1981) in Table 1. The stoichiometric mole fraction $X_s$ shifts to 0.514 and temperature $T_s$ decreases to 1872 K. Due principally to the lower temperatures, $T(X)$ on either side of $X_s$ is even more nearly linear than in Figure 19a. This piecewise linearity leads to the equivalence principle in Figure 20.

45
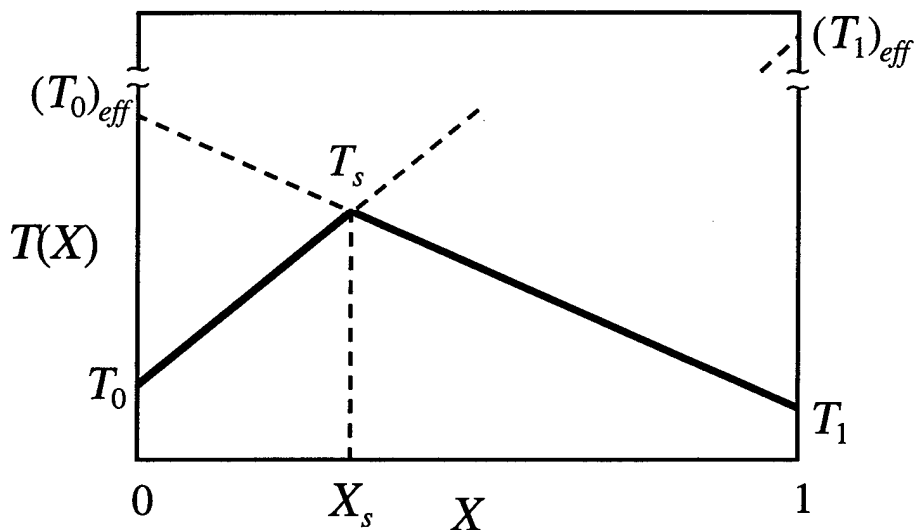
Figure 20.    Effective fluid temperatures $(T_0)_{eff}$ and $(T_1)_{eff}$ obtained by extrapolating $T(X)$ in Figure 18 on either side of the stoichimetric value $X_s$. Since a linear $T(X)$ is indicative of simple mixing without reaction as in Figure 17, wherever $X(\mathbf{x},t) > X_s$, the temperature field $T(\mathbf{x},t)$ in the reacting flow will be the same as that resulting from simple mixing in a nonreacting flow with $T_0$ replaced by $(T_0)_{eff}$. A similar equivalence holds at $X(\mathbf{x},t) < X_s$ if instead $T_1$ is replaced by $(T_1)_{eff}$.
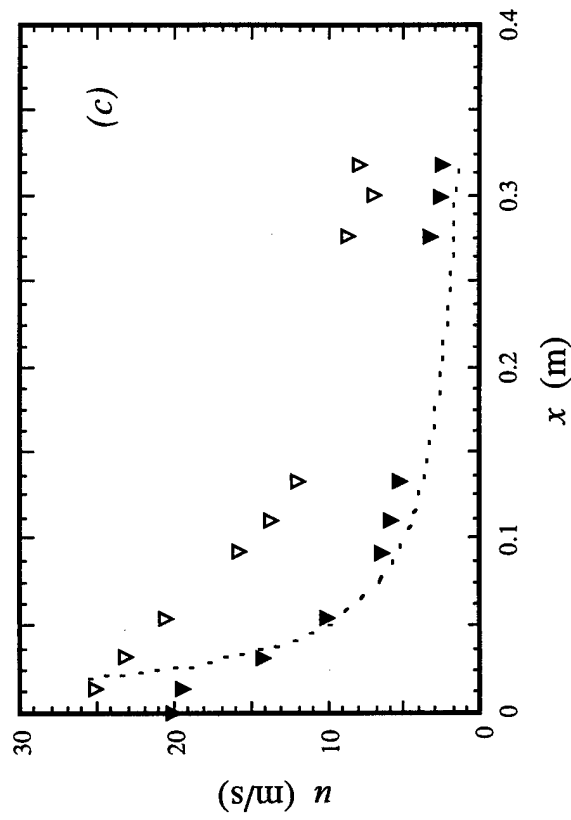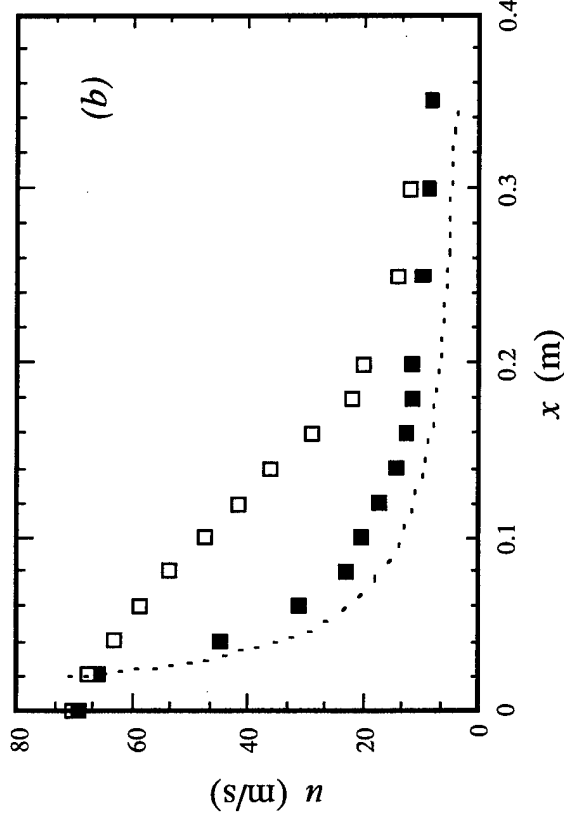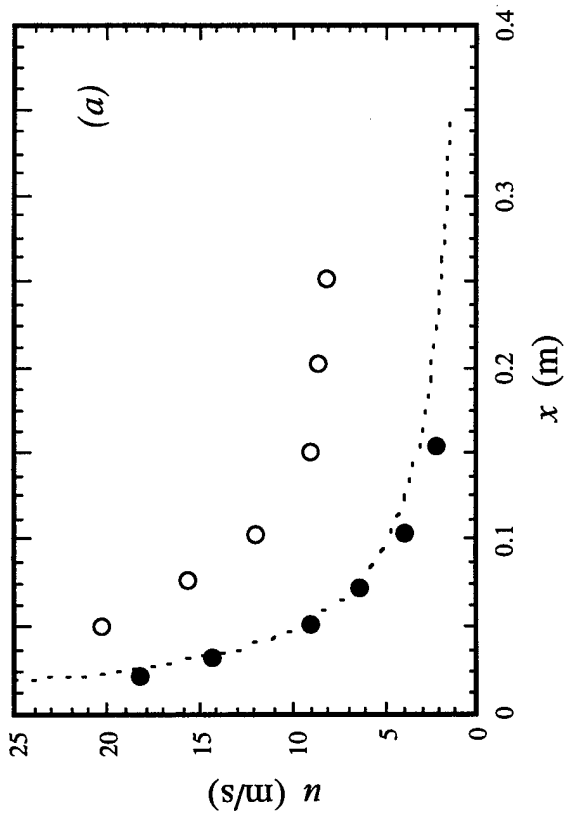
Figure 21. Comparisons of centerline velocity decay rates $u(x)$ in axisymmetric turbulent jets without heat release (*solid symbols*) and with combustion heat release (*open symbols*) under conditions for which buoyancy effects are negligible. ●, ○ Chigier & Strokin (1974) (*a*) ; ■, □ Takagi et al (1981) (*b*); ▼, ▽ Muñiz & Mungal (1995) (*c*). Dashed lines are classical scaling for nonburning jets in Eq. (7). Conditions for each case are given in Table 1.

47
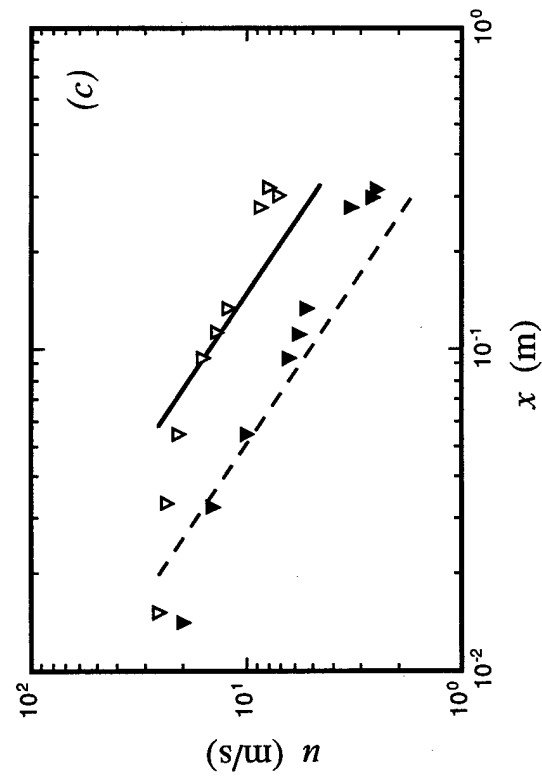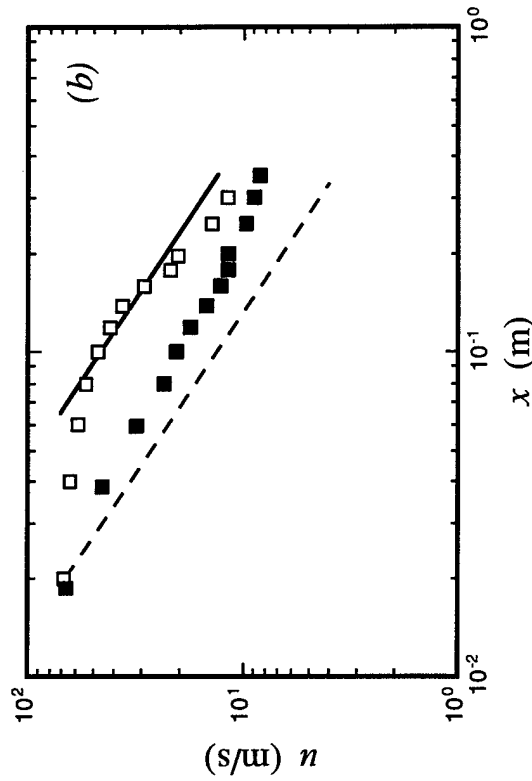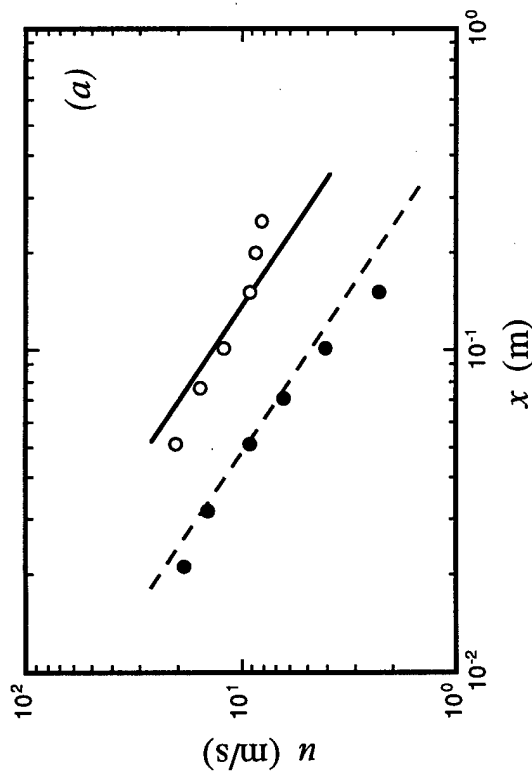
Figure 22. Comparisons of extended $d^+$ scaling law for $u(x)$ in §5.3 (*lines*) with data from Figure 21 (*symbols*) for axisymmetric turbulent jets with and without combustion heat release under otherwise identical conditions, showing: – – – scaling in Eq. (10b) without heat release; (●, ■, ▼) data without heat release; —— scaling in Eq. (10b) with heat release; (○, □, ▽) data with heat release. See legend in Figure 21. Conditions for each case are given in Table 1.

48
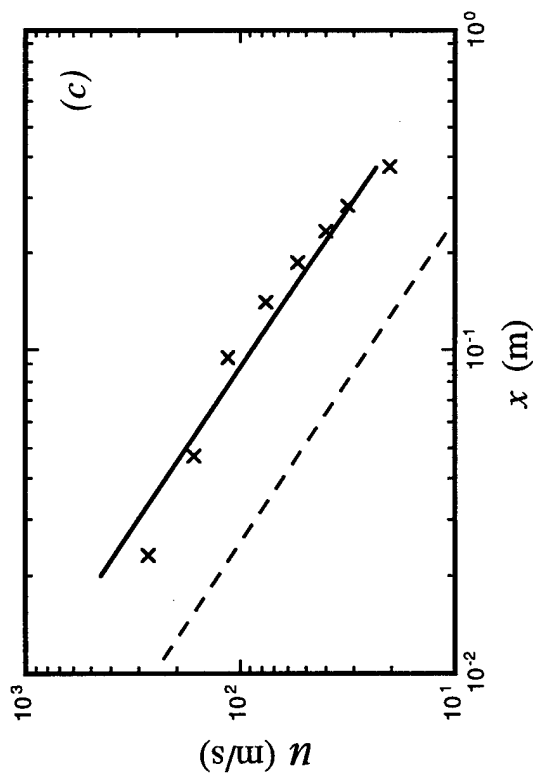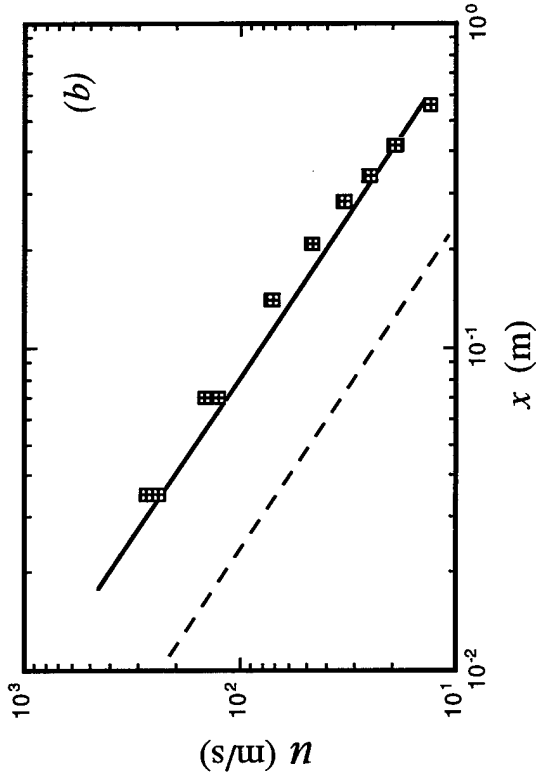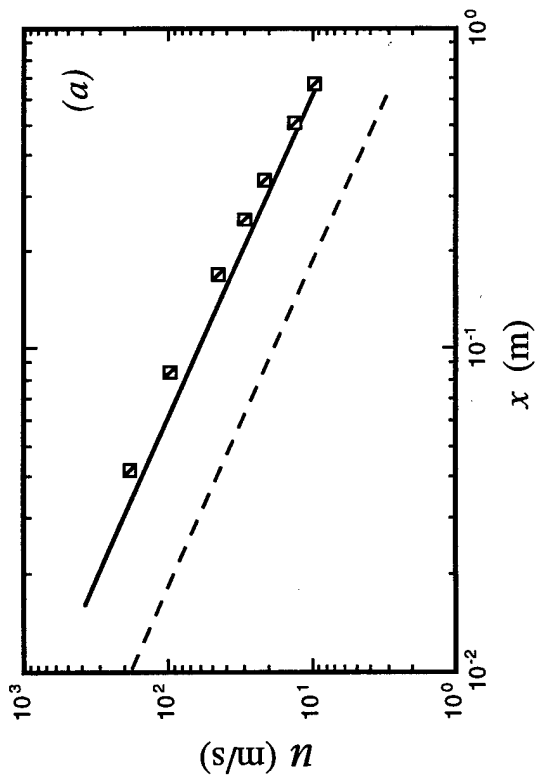
Figure 23. Comparisons of extended $d^+$ scaling law for $u(x)$ in §5.3 (*lines*) with data of Flury & Schlatter (1995) (*symbols*) for axisymmetric turbulent jet flames of hydrogen with various levels of helium dilution, under conditions for which buoyancy effects are negligible. – – – Scaling in Eq. (10$b$) without heat release; —— scaling in Eq. (10$b$) with heat release; data for 0% helium dilution ◫ ($a$); 20% helium dilution ⊞ ($b$); 40% helium dilution ⨯ ($c$). Conditions for each case are given in Table 1. Dashed lines are equivalent to classical $d^*$ scaling of Thring & Newby (1953) and Ricou & Spalding (1961) for nonexothermic jets.
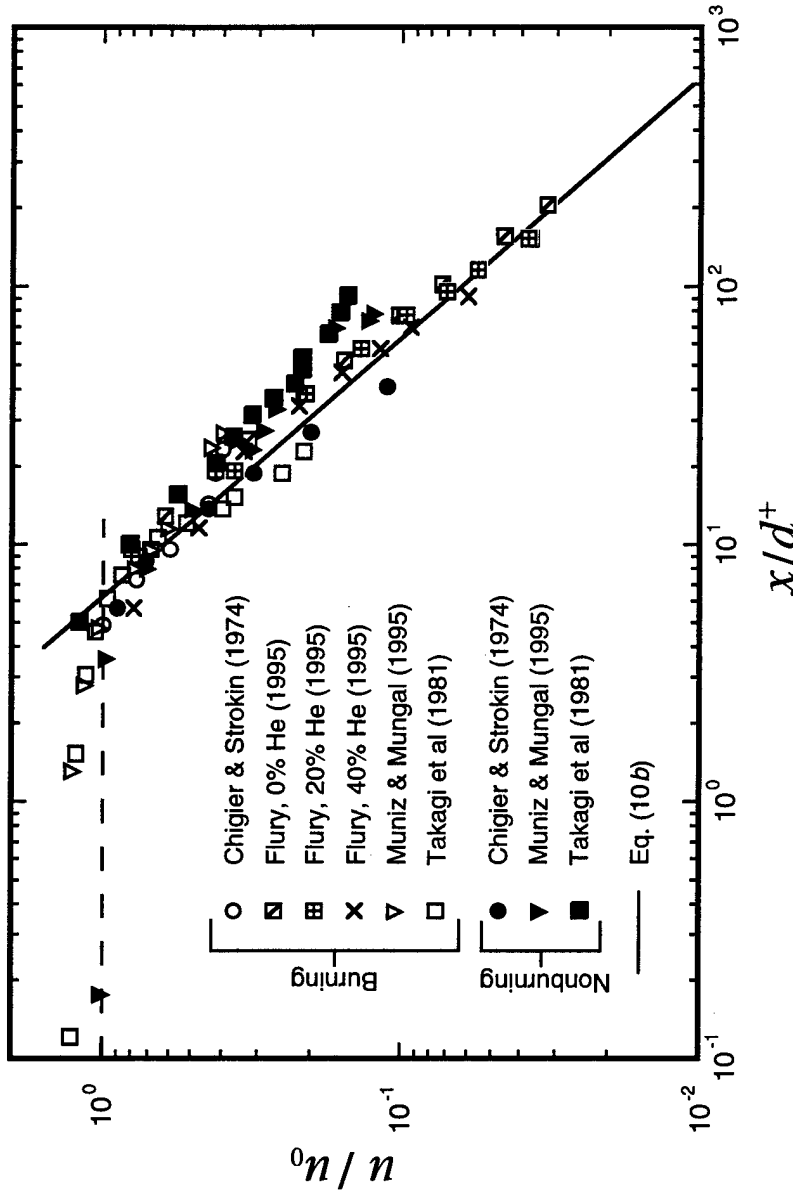
Figure 24.  Comparison of data from Figures 21 through 23 for nonburning jets (*solid symbols*) and burning jets (*open symbols*) with unified far field scaling law in Eq. (10*b*) (*solid line*) for outer velocity scale $u(x)$ in axisymmetric turbulent jets with and without combustion heat release.  For jets without heat release, $d^+$ scaling becomes identical to classical $d^*$ scaling in Eq. (7) of Thring & Newby (1953) and Ricou & Spalding (1961).  Note that agreement of present $d^+$ scaling with data from burning jets is comparable to that of classical $d^*$ scaling with data from nonburning jets.  Dashed line gives near field scaling in §5.5.
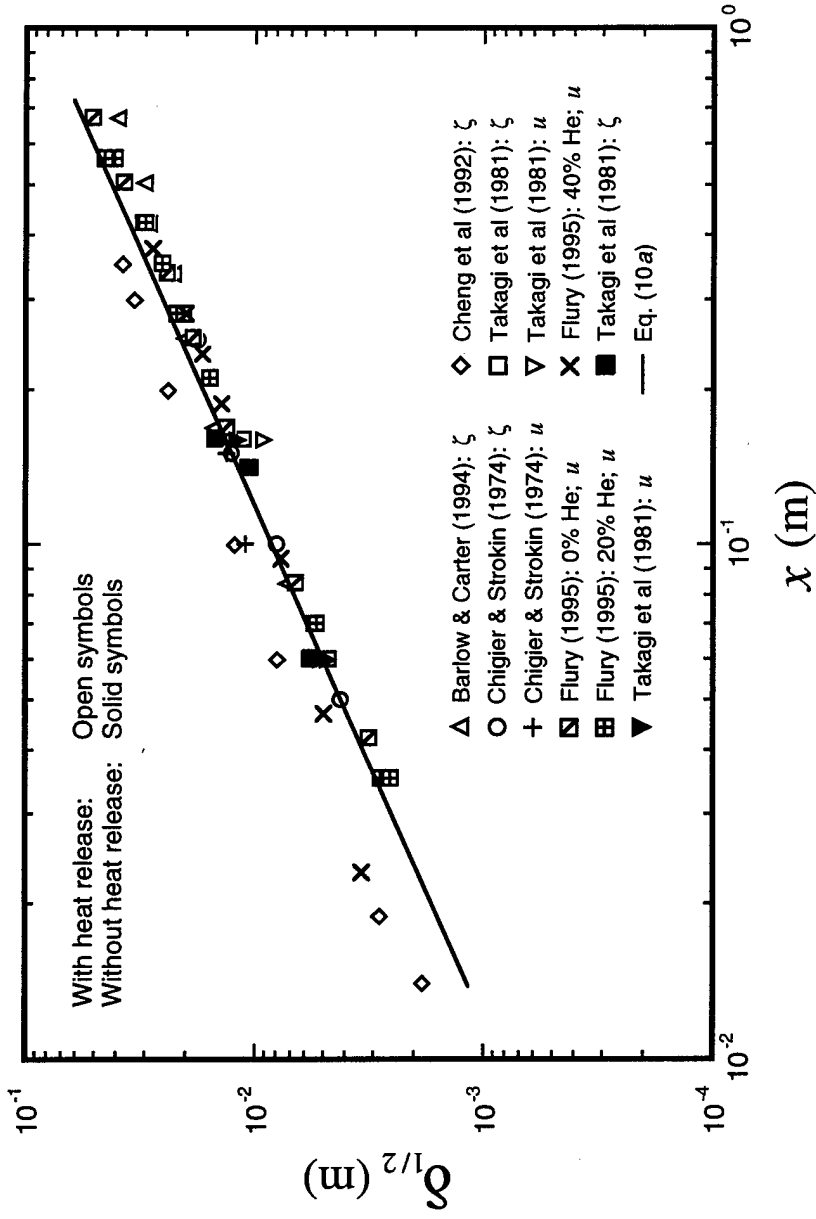
Figure 25. Comparison of outer length scale $\delta(x)$ from mean profiles of velocity $u$ and conserved scalar $\zeta$ measured in axisymmetric turbulent jets with (*open symbols*) and without (*solid symbols*) combustion heat release under conditions for which buoyancy effects are negligible. Solid line gives $\delta_{1/2} = 0.08\ x$, from $\delta$ in Eq. (10$a$) and gaussian profile shape. As in Figure 24, agreement of data from burning jets with the unified scaling in §5.3.3 is comparable to that from jets without heat release.

51
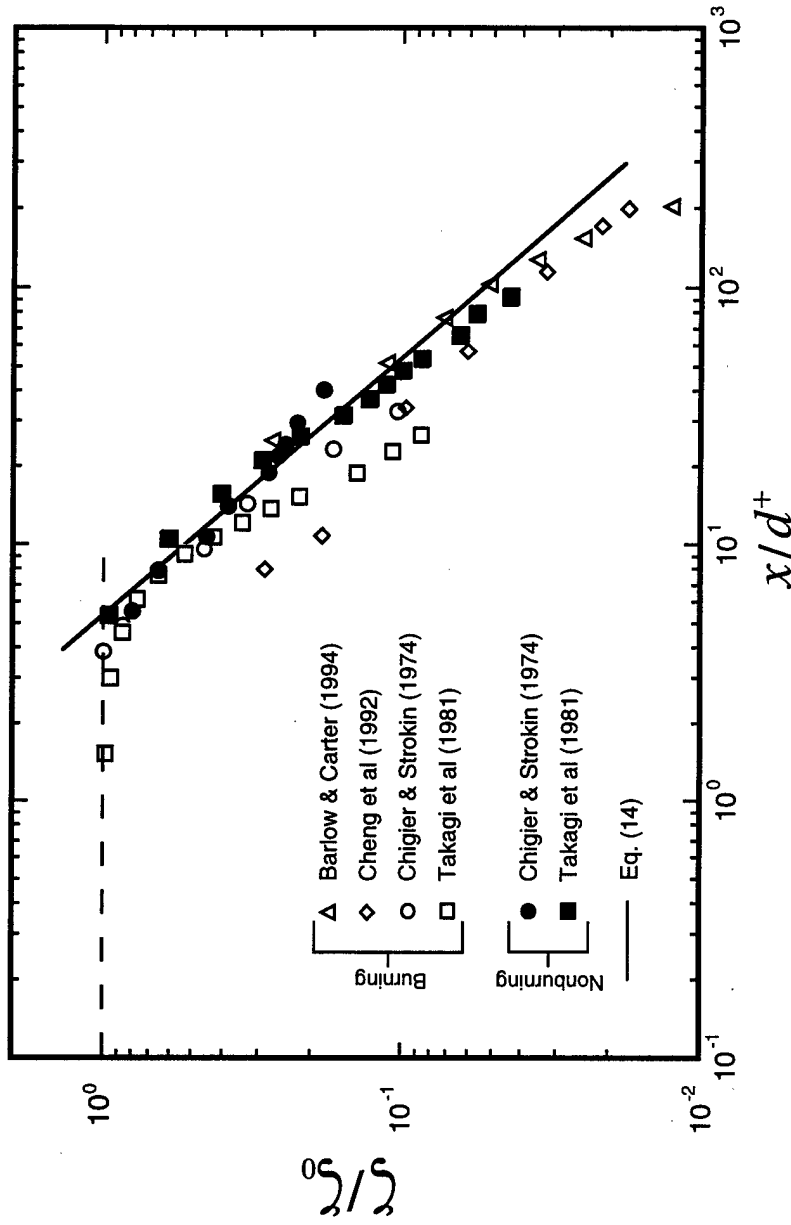
Figure 26. Comparison of data from nonburning jets (*solid symbols*) and burning jets (*open symbols*) with unified far field scaling law in Eq. (14) (*solid line*) for centerline conserved scalar decay $\zeta(x)$ in axisymmetric turbulent jets with and without combustion heat release. Dashed line gives near field scaling in §5.5.
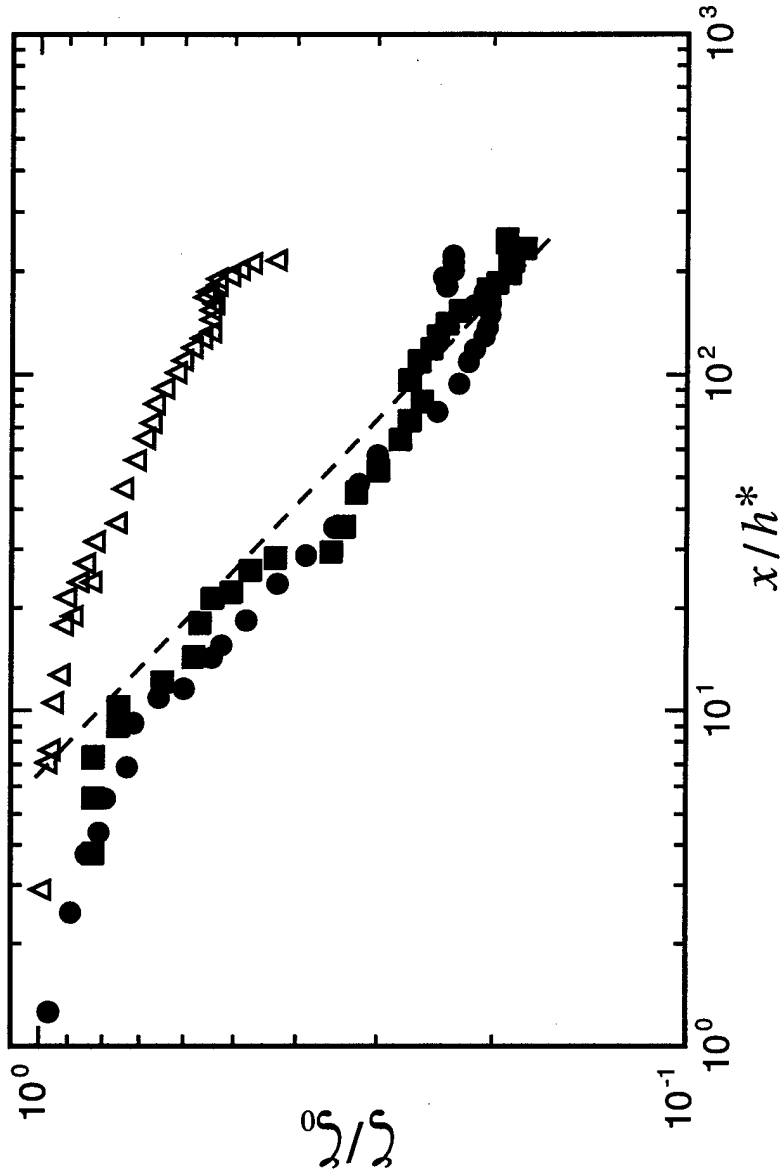
Figure 27. Comparison of centerline conserved scalar decay $\zeta(x)$ in planar turbulent jets without heat release (*solid symbols*) and with heat release (*open symbols*) in terms of classical momentum width $h^*$ of §5.4.1, under conditions for which buoyancy effects are negligible. Dashed line is $h^*$ scaling in Eq. (20) for nonburning jets. Data from Rehm & Clemens (1996, 1998). ■ He jet; ● He/$N_2$ jet; △ $H_2$/$N_2$ jet flame. Conditions are as given in Table 1. The same data are compared in Figure 28 in the extended momentum width $h^+$ of §5.4.2.
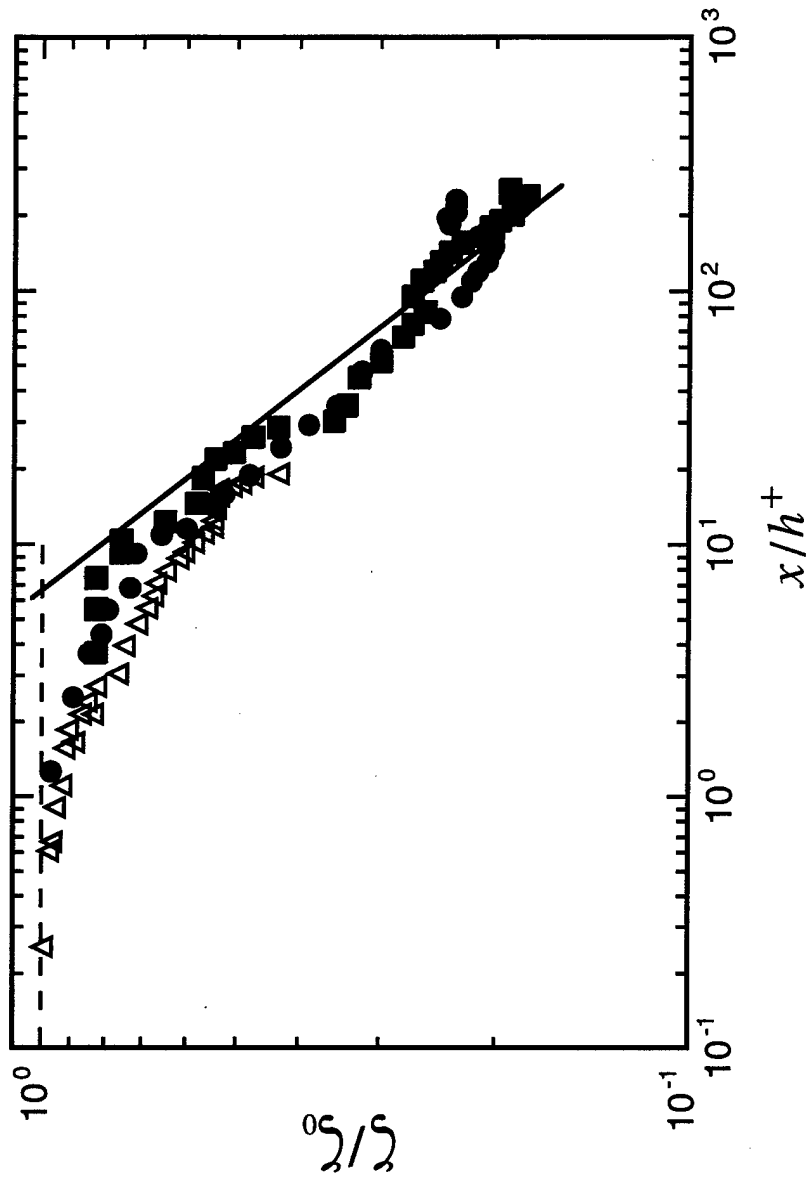
Figure 28. Comparison of data from Figure 27 for nonburning (*solid symbols*) and burning (*open symbols*) planar turbulent jets with the unified far field scaling law in Eq. (21) (*solid line*). For jets without heat release, $h^+$ scaling becomes identical to classical $h^*$ scaling in Figure 27. Agreement of present $h^+$ scaling with far field data from burning jet is comparable to that of classical $h^*$ scaling with data from nonburning jets. Dashed line gives near field scaling in §5.5.

AFOSR Contract No. F49620-95-1-0115
The University of Michigan .. .... .

Final Technical Report

## References

Barlow, R.S. & Carter, C.D. (1994) Raman/Rayleigh/LIF measurements of nitric oxide formation in turbulent hydrogen jet flames. *Comb. Flame* **9 7**, 261-280.

Blake, T.R. and McDonald, M. (1993) An examination of flame length data from vertical turbulent diffusion flames. *Comb. Flame* **9 4**, 426-432.

Cheng, T.S., Wehrmeyer, J.A. and Pitz, R.W. (1992) Simultaneous temperature and multispecies measurements in a lifted hydrogen diffusion flame. *Comb. Flame* **9 1**, 323-345.

Chigier, N.A. and Strokin, V. (1974) Mixing process in a free turbulent diffusion flame. *Comb. Sci. Tech.* **9**, 111-118.

Clemens, N.T. and Paul, P.H. (1995) Effects of heat release on the near field structure of hydrogen jet diffusion flames. *Comb. Flame* **1 0 2**, 271-284.

Crookson, R.A., Flanagan, P. and Penny, G.S. (1969) A study of free-jet and enclosed supersonic diffusion flames. *Proc. 12th Int'l Symp. Comb.* 1115-1124.

Dahm, W.J.A. and Dimotakis, P.E. (1987) Measurements of entrainment and mixing in turbulent jets. *AIAA J.* **2 5**, 1216-1223.

Drewry, J.E. (1972) Supersonic mixing and combustion of confined coaxial hydrogen-air streams. *AIAA Paper 72-1178*, American Institute of Aeronautics & Astronautics, Washington D.C.

Flury, M. and Schlatter, M. (1995) Experimental and numerical investigation of turbulent nonpremixed hydrogen flames. *1995 Joint Meeting of the German and French Sections*, The Combustion Institute, Pittsburgh.

Gutmark, E. & Wygnanski, I. (1976) The planar turbulent jet. *J. Fluid Mech.* **7 3**, 465-495.

Hawthorne, W.R., Weddel, D.S. and Hottel, H.C. (1949) Mixing and combustion in turbulent gas jets. *Proc. 3rd Int'l. Symp. Comb., Flame, and Expl. Phenom.* 266-288, Williams & Wilkins, Co., Baltimore.

Hottel, H.C. and Hawthorne, W.R. (1949) Diffusion in laminar flame jets. *Proc. 3rd Int'l. Symp. Comb., Flame, and Expl. Phenom.* 254-266, Williams & Wilkins, Co., Baltimore.

Huh, H. (1996) Shock wave enhancement of the mixing and stability limits of supersonic hydrogen-air flames. Ph.D. Thesis, The University of Michigan.

Kremer, H. (1967) Mixing in a plane free-turbulent-jet diffusion flame. *Proc. 11th Int'l. Symp. Comb.* 799-806, The Combustion Institute, Pittsburgh.

Muñiz, L. and Mungal, M.G. (1995) A PIV investigation of turbulent diffusion flames. *Paper No. WSS/CI-95F-206*, 1995 Fall Mtg., Western States Section of the Combustion Institute, The Combustion Institute, Pittsburgh.

Northam, G.B., Greenburg, I. and Byington, C.S. (1989) Evaluation of parallel injector configurations for supersonic combustion. *AIAA Paper 89-2525*, American Institute of Aeronautics & Astronautics, Washington D.C.

Rehm, J.E. and Clemens, N.T. (1996) The structure of planar hydrogen jet diffusion flames. AIAA Paper No. 96-0704, 34th Aerospace Sciences Meeting, AIAA, Washington D.C..

Rehm, J.E. and Clemens, N.T. (1998) The large scale structure of nonpremixed planar hydrogen jet flames. To appear in *Comb. Flame.*

Rhine, J.M. and Tucker, R.J. (1991) Modeling of Gas-Fired Furnaces and Other Industrial Heating Processes. McGraw-Hill.

Ricou, F.P. and Spalding, D.B. (1961) Measurements of entrainment and mixing by axisymmetrical turbulent jets. *J. Fluid Mech.* **11**, 21-32.

Savas, O. and Gollahalli, S.R. (1986) Flow structure in near-nozzle region of gas jet flames. *AIAA J.* **24**, 1137-1140.

Slutsky, S., Tamagno, J. and Trentacoste, N. (1965) Supersonic combustion in premixed hydrogen-air flows. *AIAA J* **3**, 1599-1605.

Smits, A.J., Spina, E.F., Alving, A.E., Smith, R.W., Fernando, E.M., and Donovan, J.F. (1989) A comparison of the turbulence structure of subsonic and supersonic boundary layers. *Phys. Fluids A* **1**, 1865-1875.

Sunavala, P.D., Hulsa, C. and Thring, M. (1957) Mixing and combustion in free and enclosed turbulent jet diffusion flames. *Comb. Flame* **1**, 179-193.

Tacina, K.M. and Dahm, W.J.A. (1996) Heat release effects on scaling laws for turbulent shear flows. *Bull. Am. Phys. Soc.* **41** (9), 1814 (abstract only).

Takagi, T., Shin, H-D. and Ishio, A. (1981) Properties of turbulence in turbulent diffusion flames. *Comb. Flame* **40**, 121-140.

Takeno, T. (1994) Transition and structure of jet diffusion flames. *Proc. 25th Int'l. Symp. Comb.* 1061-1073, The Combustion Institute, Pittsburgh.

Thring, M.W. and Newby, M.P. (1953) Combustion length of enclosed turbulent jet flames. *Proc. 4th Int'l. Symp. Comb.* 789-796, Williams & Wilkins, Co., Baltimore.

Wygnanski, I. and Fiedler, H. (1969) Some measurements in the self-preserving jet. *J. Fluid*

*Mech.* **38**, 577-612.

Yamashita, H., Kushida, G. and Takeno, T. (1990) A numerical study of the transition of jet diffusion flames. *Proc. Roy. Soc. Lond. Ser. A* **431**, 301.

Yule, A.J., Chigier, N.A., Ralph, S., Boulderstone, R. and Ventura, J. (1981) Combustion-transition interaction in a jet flame. *AIAA J.* **19**, 752-760.